

Accelerated Article Preview

Common human genetic variants of *APOE* impact murine COVID-19 mortality

Received: 25 September 2021

Accepted: 13 September 2022

Accelerated Article Preview

Cite this article as: Ostendorf, B. N. et al. Common human genetic variants of *APOE* impact murine COVID-19 mortality. *Nature* <https://doi.org/10.1038/s41586-022-05344-2> (2022).

Benjamin N. Ostendorf, Mira A. Patel, Jana Bilanovic, H.-Heinrich Hoffmann, Sebastian E. Carrasco, Charles M. Rice & Sohail F. Tavazoie

This is a PDF file of a peer-reviewed paper that has been accepted for publication. Although unedited, the content has been subjected to preliminary formatting. Nature is providing this early version of the typeset paper as a service to our authors and readers. The text and figures will undergo copyediting and a proof review before the paper is published in its final form. Please note that during the production process errors may be discovered which could affect the content, and all legal disclaimers apply.

Common human genetic variants of *APOE* impact murine COVID-19 mortality

Benjamin N. Ostendorf^{1,4,5*}, Mira A. Patel^{1#}, Jana Bilanovic^{1#}, H.-Heinrich Hoffmann², Sebastian E. Carrasco³, Charles M. Rice², Sohail F. Tavazoie^{1*}

¹Laboratory of Systems Cancer Biology, The Rockefeller University, New York, NY 10065, USA

²Laboratory of Virology and Infectious Disease, The Rockefeller University, New York, NY 10065, USA

³Laboratory of Comparative Pathology, Weill Cornell Medicine, Memorial Sloan Kettering Cancer Center, and Rockefeller University, New York, NY 10065, USA

⁴Department of Hematology, Oncology, and Tumor Immunology and Berlin Institute of Health, Charité-Universitätsmedizin Berlin, Germany

⁵Berlin Institute for Medical Systems Biology (BIMSB), Max Delbrück Center for Molecular Medicine, Berlin, Germany

#contributed equally

*Correspondence: bostendorf@rockefeller.edu, sohail.tavazoie@rockefeller.edu

Clinical outcomes of severe acute respiratory syndrome coronavirus 2 (SARS-CoV-2) infection are highly heterogeneous, ranging from asymptomatic infection to lethal coronavirus disease 2019 (COVID-19). The factors underlying this heterogeneity remain insufficiently understood. Genetic association studies have suggested that genetic variants contribute to the heterogeneity of COVID-19 outcomes, but the underlying potential causal mechanisms are insufficiently understood. Here we show that common variants of the Apolipoprotein E (*APOE*) gene, homozygous in approximately 3% of the world's population¹ and associated with Alzheimer's disease, atherosclerosis and anti-tumor immunity²⁻⁵, impact COVID-19 outcome in a mouse model that recapitulates increased susceptibility conferred by male sex and advanced age. Mice bearing the *APOE2* or *APOE4* variant exhibited rapid disease progression and poor survival outcomes relative to mice bearing the most prevalent *APOE3* allele. *APOE2* and *APOE4* mice exhibited increased viral loads as well as suppressed adaptive immune responses early after infection. In vitro assays demonstrated increased infection in the presence of *APOE2* and *APOE4* relative to *APOE3*, indicating that differential outcomes are mediated by differential effects of *APOE* variants on both viral infection and antiviral immunity. Consistent with these in vivo findings in mice, *APOE* genotype was associated with survival in SARS-CoV-2 infected patients in the UK Biobank (candidate variant analysis, $P = 2.6 \times 10^{-7}$). Our findings suggest *APOE* genotype to partially explain the heterogeneity of COVID-19 outcomes and warrant prospective studies to assess *APOE* genotyping as a means of identifying patients at high risk for adverse outcomes.

34 Severe acute respiratory syndrome coronavirus 2 (SARS-CoV-2) has caused the COVID-19 pandemic
35 with more than 580 million confirmed infections and 6 million deaths to date worldwide. Clinical
36 presentations of SARS-CoV-2 infection show pronounced variation, ranging from asymptomatic infection
37 to lethal disease. Several epidemiological factors have been identified that associate with adverse
38 outcome, including male sex, advanced age, select comorbidities, and genetic ancestry⁶. However, these
39 factors only partially explain the wide inter-individual clinical spectrum of SARS-CoV-2 infection. There is
40 thus a major need to identify the factors underlying susceptibility to poor outcome in COVID-19. Major
41 efforts have shown germline genetics to correlate with disease severity in COVID-19 (reviewed in⁷).
42 Amongst these, candidate gene approaches have revealed rare autosomal inborn errors of type I
43 interferon (IFN) immunity to alter type I IFN signaling *in vitro*^{8,9}. In addition, genome-wide association
44 studies have identified several genomic loci to be significantly associated with critical COVID-19<sup>10-
45 15</sup>^{10,11,13,16}. However, it remains unknown whether common germline variants causally impact the course
46 of COVID-19.

47 APOE is a secreted protein with canonical roles in lipid metabolism. Importantly, APOE has also been
48 shown to modulate immunity in different contexts, including infection and anti-tumor immunity^{2,17,18}. Two
49 single-nucleotide polymorphisms give rise to three highly prevalent variants of *APOE*, termed *APOE2*,
50 *APOE3*, and *APOE4*. The proteins encoded by these alleles differ by one or two amino acids. Forty
51 percent of the world's population carry at least one copy of either the *APOE2* or *APOE4* allele, and
52 approximately 3 % are homozygous for either *APOE2* or *APOE4*¹. The *APOE4* variant is the strongest
53 monogenetic risk factor for Alzheimer's disease^{19,20}. *APOE* variants also modulate several immune-
54 related processes, including atherosclerosis⁴ and anti-tumor immunity³, prompting us to determine
55 whether *APOE* causally modulates SARS-CoV-2 infection. Using genetic mouse models of *APOE* human
56 genetic variation as well as supportive clinical association studies, we found that the *APOE2* and *APOE4*
57 variants confer adverse outcomes in SARS-CoV-2 infection *in vivo* including reduced survival.

58 ***APOE* causally impacts murine COVID-19 outcomes**

59 To assess the impact of *APOE* germline variation on SARS-CoV-2 infection, we infected 328 *APOE*
60 knock-in mice across different ages and of both sexes with SARS-CoV-2 MA10, a mouse-adapted strain
61 of SARS-CoV-2²¹ (**Extended Data Fig. 1a-c**). In *APOE* knock-in mice, the murine *ApoE* gene is replaced
62 with one of the three human *APOE* alleles. Multivariate analysis revealed that this murine model
63 recapitulated the increased risk for poor survival conferred by male sex and those of advanced age as
64 previously shown in humans (**Fig. 1a-c**). Remarkably, *APOE* genotype also significantly impacted
65 survival, with both the *APOE2* and *APOE4* variants conferring poor survival outcomes relative to the
66 *APOE3* variant (**Fig. 1a, d**). In both male and female age-matched mice, *APOE4* mice exhibited
67 accelerated weight loss relative to the other variants (**Fig. 1e-g, j-l; Extended Data Fig. 1d**). While
68 female mice showed higher survival overall, *APOE2* and *APOE4* conferred worse survival outcomes in
69 both male and female mice (**Fig. 1h-i, m-n**). The impact was particularly pronounced in male mice, with

70 100% of *APOE4* mice succumbing to COVID-19 in contrast to approximately 30% mortality in *APOE3*
71 mice. We observed a significant interaction between *APOE* genotype and age, with the impact of *APOE*
72 on survival being more pronounced in younger mice. No significant interaction was observed for *APOE*
73 genotype and sex (**Extended Data Fig. 1e-h**). Of note, no spontaneous deaths were detected in similarly
74 aged and non-infected *APOE* knock-in mice over a comparable period, indicating that the known impact
75 of *APOE* genotype on longevity does not confound these results (**Extended Data Fig. 1i-k**). Thus, *APOE*
76 variants causally and dramatically impact the outcome of murine COVID-19.

77 ***APOE2* and *APOE4* mice exhibit accelerated COVID-19 progression**

78 To assess viral load, we performed TaqMan quantitative real-time PCR on lungs from *APOE* knock-in
79 mice on day four post infection. Consistent with faster disease progression, *APOE2* and *APOE4* mice
80 showed elevated viral loads relative to *APOE3* mice (**Fig. 2a**). These differences were already evident on
81 day two post infection (**Extended Data Fig. 2a**) and validated by SARS-CoV-2 nucleocapsid
82 immunofluorescence staining (**Fig. 2b**). Histopathological analyses on day four post infection revealed
83 pronounced lung injury in *APOE4* mice with increased bronchiolar necrosis, alveolar damage, and fibrin
84 deposition (**Fig. 2c-f, Extended Data Fig. 2b-c**). No differences were observed for inflammatory infiltrates
85 in the pulmonary interstitium and vessels in *APOE2* or *APOE4* mice in comparison with *APOE3* mice
86 (**Extended Data Fig. 2d-h**). These results indicate accelerated COVID-19 progression in *APOE2* and
87 *APOE4* mice relative to *APOE3*, with histopathologic features evident by day four primarily in *APOE4*
88 mice.

89 ***APOE* genotype modulates COVID-19 outcome by impacting antiviral immunity 90 and viral infection**

91 We next performed transcriptional profiling of homogenized lungs of non-infected *APOE* knock-in mice
92 and on days two and four post infection with SARS-CoV-2 MA10 (**Fig. 3a**). To identify clusters of highly
93 correlated genes and relate their expression to genotype and timepoint relative to infection, we employed
94 weighted gene co-expression network analysis (WGCNA; see methods)²². WGCNA revealed five
95 modules of co-expressed genes that were significantly correlated with *APOE* genotype, and ten modules
96 correlated with timepoint relative to infection (**Fig. 3b**). Assessment of the trajectories of the eigengene of
97 these modules (a metric summarizing the weighted overall expression of a module) revealed modules
98 that became specifically up- or downregulated in *APOE3* relative to *APOE2* and *APOE4* mice during
99 disease progression, most pronounced for modules greenyellow/midnightblue and black, respectively
100 (**Fig. 3c, Extended Data Fig. 3a**), and validated in an independent cohort of mice (**Extended Data Fig.**
101 **3b-c**). Correlations of the greenyellow, midnightblue and pink modules with *APOE* genotype were also
102 significant in an independent third cohort of young female mice (**Extended Data Fig. 3d-e**). Pathway
103 analysis of the black module that exhibited higher expression in *APOE2* and *APOE4* relative to *APOE3*
104 mice on day four revealed enrichment of genes implicated in blood coagulation and hemostasis,
105 abnormalities of which are frequent in severe COVID-19²³ (**Extended Data Fig. 3f-g**). Strikingly, analysis

106 of the modules that exhibited downregulation in *APOE2* and *APOE4* mice relative to *APOE3* on day four
107 (greenyellow, midnightblue, yellow) showed enrichment of genes implicated in T and B cell activation as
108 well as positive immune response regulation (**Extended Data Fig. 3h-o**). Immunofluorescence staining
109 indicated overall similar levels of CD45⁺ leukocytes in *APOE2* and *APOE4* relative to *APOE3* mice
110 (**Extended Data Fig. 3p**). These data are consistent with dampened adaptive immunity during early
111 response to COVID-19 in *APOE2* and *APOE4* relative to *APOE3* mice.

112 Consistent with these findings, flow cytometry on dissociated lungs on day four post infection confirmed
113 an expansion of myeloid cells and relative depletion of lymphoid cells in the lungs of both *APOE2* and
114 *APOE4* relative to *APOE3* mice (**Fig. 3d, Extended Data Fig. 4a-b**). In humans with severe COVID-19,
115 depletion of lymphoid subsets has also been observed in the peripheral blood^{24,25}. To assess whether
116 these changes were recapitulated by our animal model, we performed flow cytometry on peripheral blood
117 of *APOE* knock-in mice. While total leukocyte numbers were not significantly different between *APOE*
118 genotypes, both *APOE2* and *APOE4* mice showed expansion of myeloid cells mainly driven by Ly6G⁺
119 neutrophils with concomitant contraction of all major lymphoid populations (**Extended Data Fig. 4c-g**).
120 These data are consistent with the reported elevation of myeloid/lymphoid ratios in patients with adverse
121 COVID-19 outcomes^{24,25} and suggest that adaptive immune responses are blunted in *APOE2* and
122 *APOE4* mice during early COVID-19 progression.

123 To further profile the immunological response in *APOE* knock-in mice during COVID-19, we performed
124 single cell RNA-sequencing (scRNAseq) on a total of 41,500 cells (post-filtering) from 29 mice across all
125 three genotypes with and without COVID-19 (**Extended Data Fig. 5a-d**). Infected mice showed a marked
126 expansion of myeloid cells, which, consistent with our flow cytometry data, was more prominent in *APOE2*
127 and *APOE4* relative to *APOE3* mice (**Fig. 3e-f, Extended Data Fig. 6**). To assess changes in the
128 functional status of cell clusters, we performed gene set enrichment analysis. Strikingly, *APOE2* mice
129 showed more pronounced enrichment of various immune-related pathways relative to *APOE3* in
130 comparison to *APOE4* relative to *APOE3* mice (**Fig. 3g**). In humans, hyperactivation of proinflammatory
131 signaling has been implicated in adverse outcomes^{24,26}. We therefore hypothesized that despite a similar
132 change in immune subset abundances during early infection, antiviral immune responses might diverge
133 between *APOE2* and *APOE4* mice over the course of infection. To test this, we assessed the generation
134 of virus spike-specific CD8⁺ T cells during infection (**Fig. 3h**). The fraction of virus spike-specific CD8⁺ T
135 cells as assessed by tetramer staining was significantly larger in *APOE4* relative to *APOE3* and *APOE2*
136 mice, consistent with *APOE4* mice eventually mounting more effective adaptive antiviral immunity than
137 *APOE2* mice (**Fig. 3i-j**). These data indicate that while both *APOE2* and *APOE4* mice initially exhibited
138 blunted adaptive immune responses, *APOE4* mice generated more robust antiviral T cell responses in
139 later stages of infection, which emerged after pathological tissue damage had occurred.

140 We next assessed whether *APOE* directly impacts viral infection, potentially explaining the emergence of
141 differences in viral titer and immune responses early upon infection. Remarkably, recombinant *APOE3*,
142 but not recombinant *APOE2* or *APOE4*, significantly suppressed infection of Huh-7.5 cells *in vitro* (**Fig.**

143 **3k)**. In sum, these data indicate that adverse outcomes in *APOE2* and *APOE4* mice are driven by both
144 enhanced viral infection and dampened adaptive antiviral immunity.

145 ***APOE* genotype associates with survival in COVID-19 patients**

146 To assess the impact of *APOE* genotype on COVID-19 outcome in humans, we analyzed participants of
147 the UK Biobank²⁷. Overall distribution of *APOE* genotype in 402,763 UK Biobank participants was
148 comparable to similarly aged individuals in the ARIC study²⁸, with approximately 40% carrying at least
149 one copy of the *APOE2* or *APOE4* allele (**Extended Data Fig. 7a, b**). Consistent with previous reports
150 carried out at earlier times during the pandemic^{29,30}, we observed a moderate enrichment of *APOE4*
151 homozygosity in participants with positive versus negative test results and in participants with positive test
152 results versus the remaining participants (**Extended Data Fig. 7c, d**). There was no significant difference
153 in *APOE* genotype distribution between patients with a positive test regarding the test origin (inpatient
154 versus outpatient; **Extended Data Fig. 7e**).

155 We next performed survival analysis of patients with confirmed SARS-CoV-2 infection. Consistent with
156 known epidemiological observations, multivariate analysis confirmed male sex and advanced age to
157 confer adverse survival outcomes (**Fig. 4a-c**). Strikingly, homozygous *APOE4* patients also exhibited poor
158 survival with a more than two-fold increased hazard ratio for death relative to *APOE3* homozygous
159 patients (**Fig. 4a, d**). Homozygous *APOE2* patients also experienced an increased hazard ratio for death
160 that did not reach statistical significance (**Fig. 4a, d**). The association between *APOE* genotype and
161 survival remained significant upon adjustment for the first ten principal components of genetic variation,
162 indicating population structure to be unlikely to account for this association (**Extended Data Fig. 8a-c**).
163 Consistently, the association of *APOE* with COVID-19 was maintained upon restriction of the analysis to
164 individuals of European ancestry (**Extended Data Fig. 8d-g**). No significant association of *APOE*
165 genotype with survival was detected over a similar period prior to the start of the COVID-19 pandemic,
166 indicating that the known association of *APOE* genotype with longevity also does not confound these
167 results (**Extended Data Fig. 8h**). Overall, these results are consistent with our animal studies that
168 demonstrate a causal role of *APOE* genotype in modulating murine COVID-19 outcome. While the
169 present work was in revision, an independent study validated the epidemiologic association of *APOE4*
170 with adverse outcomes in COVID-19 in the large FINNGEN cohort³¹.

171 **Discussion**

172 The COVID-19 pandemic has had a devastating impact on public health, but individual outcomes are
173 markedly heterogeneous. Comprehensive efforts have been made to uncover the genetic basis of
174 COVID-19 outcome. These efforts were either carried out using genome-wide or candidate gene
175 approaches and identified genetic variants and regions epidemiologically associated with COVID-19
176 outcome^{8,10-12,14,15,32}. However, whether common germline variants could causally modulate COVID-19
177 outcomes *in vivo* is unknown. In this work, we undertook a reverse genetic approach and specifically
178 focused on *APOE* variants given their previously established roles in modulating immunity. By employing

179 genetic mouse models of human *APOE* germline variation, we established a causal link between *APOE*
180 genotype and COVID-19 outcome in mice, supported by clinical association data in humans. Importantly,
181 our focused genetic and biochemical studies of these *APOE* variants led us to assess their
182 epidemiological associations with human outcomes. While previous genome-wide association studies for
183 COVID-19 critical illness have not detected associations with variants in *APOE* that reached genome-
184 wide significant threshold levels, our data on *APOE* variant association with survival in COVID-19 patients
185 in a candidate analysis are supported by the reverse genetic approach in mice, suggesting a potential
186 causal relationship between *APOE4* genotype and COVID-19 outcome in human disease.

187 We uncovered two mechanisms underlying *APOE*-genotype dependent differences in murine COVID-19
188 outcomes: Both *APOE2* and *APOE4* mice showed impaired immune responses during early infection.
189 Single cell transcriptional profiling indicated hyperactivation of proinflammatory signaling in *APOE2*
190 relative to *APOE3* and *APOE4* mice. In addition, *APOE4* mice exhibited increased expansion of virus-
191 specific CD8⁺ T cells during later stages of infection, indicating that antiviral T cell responses diverge
192 between *APOE2* and *APOE4* during later infection stages. In addition to these effects on antiviral
193 immunity, we found that recombinant *APOE3*, but not recombinant *APOE2* or *APOE4*, inhibited viral
194 infection in vitro. These findings are consistent with a prior study demonstrating increased infection of
195 *APOE4* relative to *APOE3* neurons and astrocytes³³. While this past study's findings could be interpreted
196 as *APOE4* enhancing infection of neurons and astrocytes relative to *APOE3*, we interpret our findings as
197 *APOE3* repressing infection in contrast to *APOE2* and *APOE4*. Our data indicate that adverse outcomes
198 in *APOE2* and *APOE4* mice may be mediated by both enhanced viral infection and maladaptive immunity
199 during early infection, with *APOE4* mice ultimately generating more robust antiviral T cell immunity than
200 *APOE2* mice.

201 It will be important to further dissect the mechanistic basis of how these variants exert detrimental effects
202 on COVID-19 outcome at a molecular level in future studies. *APOE* has been shown to directly modulate
203 both innate and adaptive immune responses^{2,34,35}, providing potential clues towards its molecular
204 mechanism of action in immune modulation. In addition, a genetic screen identified cholesterol
205 metabolism to impact SARS-CoV-2 infection³⁶⁻³⁸, and SARS-CoV-2 may bind directly to *APOE*³⁹,
206 providing starting points for additional mechanistic studies focused on how *APOE* impacts viral infection.
207 It is important to note that the effects of *APOE* variants seem to be disease-context specific, with *APOE2*
208 and *APOE4* conferring beneficial and/or detrimental outcomes depending on phenotype^{3,19,20,40-42}.
209 Moreover, the dual impact of *APOE* genetic variation on COVID-19 and Alzheimer's outcomes has
210 implications for understanding the neurocognitive changes imparted by both disorders.

211 Our findings have several potential clinical implications. Firstly, prospective clinical studies are warranted
212 to determine if *APOE* genotyping could be used for risk stratification in SARS-CoV-2 and perhaps other
213 virus infections. Such genotyping may allow future patients to benefit from more aggressive preventative
214 and therapeutic approaches, including early booster vaccinations, anti-viral drugs and monoclonal
215 antibody therapies. The impact of vaccination or prior infection history on *APOE* genotype dependence of

216 COVID-19 outcomes will need to be determined. Additionally, it will be important to assess vaccination
217 efficacy in individuals of distinct *APOE* genotypes. More generally, our work confirms that common
218 genetic variation can give rise to heterogeneous outcomes of COVID-19.

219 References

- 220 1. Farrer, L. A. *et al.* Effects of age, sex, and ethnicity on the association between apolipoprotein E genotype and Alzheimer
221 disease. A meta-analysis. APOE and Alzheimer Disease Meta Analysis Consortium. *JAMA* **278**, 1349–56 (1997).
- 222 2. Tavazoie, M. F. *et al.* LXR/ApoE Activation Restricts Innate Immune Suppression in Cancer. *Cell* **172**, 825–840.e18 (2018).
- 223 3. Ostendorf, B. N. *et al.* Common germline variants of the human APOE gene modulate melanoma progression and survival.
224 *Nature Medicine* **26**, 1048–1053 (2020).
- 225 4. Mahley, R. W. Apolipoprotein E: from cardiovascular disease to neurodegenerative disorders. *J Mol Med (Berl)* **94**, 739–46
226 (2016).
- 227 5. Shi, Y. & Holtzman, D. M. Interplay between innate immunity and Alzheimer disease: APOE and TREM2 in the spotlight. *Nat*
228 *Rev Immunol* **18**, 759–772 (2018).
- 229 6. Williamson, E. J. *et al.* Factors associated with COVID-19-related death using OpenSAFELY. *Nature* **584**, 430–436 (2020).
- 230 7. Zhang, Q., Bastard, P., Cobat, A. & Casanova, J.-L. Human genetic and immunological determinants of critical COVID-19
231 pneumonia. *Nature* 1–15 (2022) doi:10.1038/s41586-022-04447-0.
- 232 8. Zhang, Q. *et al.* Inborn errors of type I IFN immunity in patients with life-threatening COVID-19. *Science* **370**, (2020).
- 233 9. Asano, T. *et al.* X-linked recessive TLR7 deficiency in ~1% of men under 60 years old with life-threatening COVID-19. *Sci.*
234 *Immunol.* **6**, eabl4348 (2021).
- 235 10. The Severe Covid-19 GWAS Group. Genomewide Association Study of Severe Covid-19 with Respiratory Failure. *New*
236 *England Journal of Medicine* **383**, 1522–1534 (2020).
- 237 11. Pairo-Castineira, E. *et al.* Genetic mechanisms of critical illness in COVID-19. *Nature* **591**, 92–98 (2021).
- 238 12. COVID-19 Host Genetics Initiative *et al.* Mapping the human genetic architecture of COVID-19. *Nature* **600**, 472–477 (2021).
- 239 13. Nakanishi, T. *et al.* Age-dependent impact of the major common genetic risk factor for COVID-19 on severity and mortality.
240 *Journal of Clinical Investigation* **131**, e152386 (2021).
- 241 14. Kousathanas, A. *et al.* Whole-genome sequencing reveals host factors underlying critical COVID-19. *Nature* **607**, 97–103
242 (2022).
- 243 15. Pathak, G. A. *et al.* A first update on mapping the human genetic architecture of COVID-19. *Nature* **608**, E1–E10 (2022).
- 244 16. COVID-19 Host Genetics Initiative. Mapping the human genetic architecture of COVID-19. *Nature* 1–8 (2021)
245 doi:10.1038/s41586-021-03767-x.
- 246 17. Ludewig, B. *et al.* Hypercholesterolemia Exacerbates Virus-Induced Immunopathologic Liver Disease Via Suppression of
247 Antiviral Cytotoxic T Cell Responses. *The Journal of Immunology* **166**, 3369–3376 (2001).
- 248 18. Toledo, A., Monzón, J. D., Coleman, J. L., Garcia-Monco, J. C. & Benach, J. L. Hypercholesterolemia and ApoE deficiency
249 result in severe infection with Lyme disease and relapsing-fever *Borrelia*. *Proceedings of the National Academy of Sciences*
250 **112**, 5491–5496 (2015).
- 251 19. Strittmatter, W. J. *et al.* Apolipoprotein E: high-avidity binding to beta-amyloid and increased frequency of type 4 allele in late-
252 onset familial Alzheimer disease. *Proc Natl Acad Sci U S A* **90**, 1977–81 (1993).
- 253 20. Corder, E. H. *et al.* Protective effect of apolipoprotein E type 2 allele for late onset Alzheimer disease. *Nat Genet* **7**, 180–4
254 (1994).
- 255 21. Leist, S. R. *et al.* A Mouse-Adapted SARS-CoV-2 Induces Acute Lung Injury and Mortality in Standard Laboratory Mice. *Cell*
256 **183**, 1070–1085.e12 (2020).
- 257 22. Langfelder, P. & Horvath, S. WGCNA: an R package for weighted correlation network analysis. *BMC Bioinformatics* **9**, 559
258 (2008).
- 259 23. Perico, L. *et al.* Immunity, endothelial injury and complement-induced coagulopathy in COVID-19. *Nat Rev Nephrol* **17**, 46–64
260 (2021).

- 261 24. Lucas, C. *et al.* Longitudinal analyses reveal immunological misfiring in severe COVID-19. *Nature* **584**, 463–469 (2020).
- 262 25. Mathew, D. *et al.* Deep immune profiling of COVID-19 patients reveals distinct immunotypes with therapeutic implications.
- 263 *Science* **369**, eabc8511 (2020).
- 264 26. Lee, J. S. *et al.* Immunophenotyping of COVID-19 and influenza highlights the role of type I interferons in development of
- 265 severe COVID-19. *Sci. Immunol.* **5**, eabd1554 (2020).
- 266 27. Sudlow, C. *et al.* UK Biobank: An Open Access Resource for Identifying the Causes of a Wide Range of Complex Diseases of
- 267 Middle and Old Age. *PLOS Medicine* **12**, e1001779 (2015).
- 268 28. Blair, C. K. *et al.* APOE genotype and cognitive decline in a middle-aged cohort. *Neurology* **64**, 268–76 (2005).
- 269 29. Ser, T. del *et al.* Residence, Clinical Features, and Genetic Risk Factors Associated with Symptoms of COVID-19 in a Cohort
- 270 of Older People in Madrid. *GER* **67**, 281–289 (2021).
- 271 30. Kuo, C.-L. *et al.* APOE ϵ 4 Genotype Predicts Severe COVID-19 in the UK Biobank Community Cohort. *The Journals of*
- 272 *Gerontology: Series A* **75**, 2231–2232 (2020).
- 273 31. Kurki, S. N. *et al.* APOE ϵ 4 associates with increased risk of severe COVID-19, cerebral microhaemorrhages and post-COVID
- 274 mental fatigue: a Finnish biobank, autopsy and clinical study. *Acta Neuropathologica Communications* **9**, 199 (2021).
- 275 32. Kosmicki, J. A. *et al.* Pan-ancestry exome-wide association analyses of COVID-19 outcomes in 586,157 individuals. *The*
- 276 *American Journal of Human Genetics* **108**, 1350–1355 (2021).
- 277 33. Wang, C. *et al.* ApoE-Isoform-Dependent SARS-CoV-2 Neurotropism and Cellular Response. *Cell Stem Cell* **28**, 331-342.e5
- 278 (2021).
- 279 34. Bonacina, F. *et al.* Myeloid apolipoprotein E controls dendritic cell antigen presentation and T cell activation. *Nat Commun* **9**,
- 280 3083 (2018).
- 281 35. Laskowitz, D. T., Lee, D. M., Schmechel, D. & Staats, H. F. Altered immune responses in apolipoprotein E-deficient mice. *J.*
- 282 *Lipid Res.* **41**, 613–620 (2000).
- 283 36. Wang, R. *et al.* Genetic Screens Identify Host Factors for SARS-CoV-2 and Common Cold Coronaviruses. *Cell* **184**, 106-
- 284 119.e14 (2021).
- 285 37. Schneider, W. M. *et al.* Genome-Scale Identification of SARS-CoV-2 and Pan-coronavirus Host Factor Networks. *Cell* **184**,
- 286 120-132.e14 (2021).
- 287 38. Hoffmann, H.-H. *et al.* Functional interrogation of a SARS-CoV-2 host protein interactome identifies unique and shared
- 288 coronavirus host factors. *Cell Host & Microbe* **29**, 267-280.e5 (2021).
- 289 39. Yin, Y., Sheng, Y., Wang, M., Ma, Y. & Ding, H. Interaction of serum proteins with SARS-CoV-2 RBD. *Nanoscale* (2021)
- 290 doi:10.1039/D1NR02687A.
- 291 40. Wozniak, M. A. *et al.* Apolipoprotein E- ϵ 4 protects against severe liver disease caused by hepatitis C virus. *Hepatology* **36**,
- 292 456–463 (2002).
- 293 41. Exel, E. van *et al.* Effect of APOE ϵ 4 allele on survival and fertility in an adverse environment. *PLOS ONE* **12**, e0179497
- 294 (2017).
- 295 42. Burt, T. D. *et al.* Apolipoprotein (apo) E4 enhances HIV-1 cell entry in vitro, and the APOE ϵ 4/ ϵ 4 genotype accelerates HIV
- 296 disease progression. *Proceedings of the National Academy of Sciences* **105**, 8718–8723 (2008).

297 **Figure legends**

298 **Fig. 1 | APOE variants modulate outcome of murine SARS-CoV-2 MA10 infection.** **a**, Multivariate

299 analysis of the impact of age, sex, and APOE genotype on survival of SARS-CoV-2 MA10-infected APOE

300 knock-in mice (P values according to multivariable Cox proportional hazards model; n = 128, 82, and 118

301 for APOE2, APOE3, and APOE4, respectively; data pooled from 13 independent experiments). **b-d**,

302 Survival of combined male and female SARS-CoV-2 MA10-infected APOE-knock-in mice stratified by age

303 (cutoff: 30 weeks) (**b**), sex (**c**), and APOE genotype (**d**) (P values according to log-rank tests). **e-n**, Age

304 distribution (**e**, **j**), weight course (**f**, **k**), weight on day 4 post infection (**g**, **l**), survival (**h**, **m**) and hazard

305 ratios (i, n) of male (e-i) versus female (j-n) *APOE*-knock-in mice from (a) stratified by *APOE* genotype (P
306 values according to Kruskal-Wallis-test (e, j), two-sided t-tests (g, l), log-rank test (h, m), and Cox
307 proportional hazard models (i, n); note that (f) and (k) show group averages but some animals died or
308 were censored for tissue harvest during the course of the experiment). Error bars in a, i, and n indicate
309 95% confidence intervals. Error bars in e, f, j, and k indicate standard error of the mean. Boxplot whiskers
310 in g and l extend to the smallest and largest value within 1.5 × interquartile ranges of the hinges, and box
311 centre and hinges indicate median and first and third quartiles, respectively. n, sample size; HR, hazard
312 ratio for death.

313 **Fig. 2 | *APOE2* and *APOE4* mice exhibit accelerated progression of COVID-19 relative to *APOE3***
314 **mice. a**, TaqMan qPCR for SARS-CoV-2 N1 in homogenized lungs from *APOE* knock-in mice on day 4
315 post infection with SARS-CoV-2 MA10 (data pooled from two experiments; P values according to two-
316 sided Mann-Whitney test; n = 15, 20, 18 for *APOE2*, *APOE3*, and *APOE4*, respectively). **b**,
317 Immunofluorescence staining for SARS-CoV-2 nucleocapsid in lungs of *APOE* knock-in mice on day 4
318 after infection with SARS-CoV-2 MA10 (P values according to two-sided Mann-Whitney tests; n = 10, 15,
319 10 for *APOE2*, *APOE3*, and *APOE4*, respectively). Images show representative sections; scale bar, 100
320 μm. **c-f**, Histopathologic scoring of bronchiolar necrosis (**c**), alveolar damage (**d**), and fibrin deposition (**e**)
321 in lungs from *APOE* knock-in mice on day 4 post infection with SARS-CoV-2 MA10 (data pooled from two
322 independent experiments; n = 18, 22, 15 for *APOE2*, *APOE3*, and *APOE4*, respectively; P values
323 according to two-sided Mann Whitney tests). **f**, Representative images for (c-e). Black arrowheads,
324 bronchiolar epithelial necrosis; inset asterisks, fibrin; white arrowheads, interstitial and perivascular
325 inflammation; inset arrows, endothelialitis. Scale bars, 1000μm (top row) and 400μm (middle and bottom
326 rows). Boxplot whiskers in (a) and (b) extend to the smallest and largest value within 1.5 × interquartile
327 ranges of the hinges, and box centre and hinges indicate median and first and third quartiles,
328 respectively.

329 **Fig. 3 | *APOE* genotype impacts COVID-19 progression through immune modulation and altered**
330 **viral infection. a**, Schematic for transcriptional profiling of lungs from SARS-CoV-2 MA10-infected mice.
331 **b**, Correlation of module eigengenes with time after infection and *APOE* genotype ordered by its impact
332 on COVID-19 survival ($E3 > E2 > E4$); stars indicate significant correlations (Pearson correlation tests). **c**,
333 Module eigengene trajectories for modules significantly correlating with *APOE* genotype (n = 4 ($E2/d0$;
334 $E3/d2$), 3 ($E4/d0$), 6 ($E2/d2$), 5 ($E4/d2$; $E3/d4$; $E4/d4$), and 7 ($E2/d4$)). **d**, Flow cytometry for indicated cells
335 in lungs of *APOE* knock-in mice on day 4 post infection (n = 21, 15, 20 for *APOE2*, *APOE3*, and *APOE4*,
336 respectively; data pooled from two independent experiments; P values according to one-tailed t-tests). **e-**
337 **f**, Density plots of 41,500 RNA-sequenced lung cells from *APOE* knock-in mice stratified by infection
338 status (**e**) or *APOE* genotype in infected mice (**f**). **g**, Gene set enrichment analysis for grouped clusters
339 from (f); grey boxes indicate no significant enrichment. **h**, Representative flow cytometry plots of tetramer⁺
340 CD8⁺ T cells on days 4 and 11 post infection (independent experiments). **i**, Proportion of tetramer⁺ CD8⁺
341 cells on day 11 post infection (n=14, 22, 17 for *APOE2*, *APOE3*, and *APOE4*, respectively; data pooled

342 from two independent experiments, P values according to two-tailed t-tests; note that some mice died
343 during the course of infection). **j**, Representative samples for (i). **k**, Fraction of infected cells after
344 incubation with SARS-CoV-2 in the presence of the indicated proteins (n = 10 per group; representative of
345 three independent experiments; P values according to two-tailed t tests). Boxplot whiskers in d, i and k
346 extend to the smallest and largest value within 1.5 × interquartile ranges of the hinges, and box centre
347 and hinges indicate median and first and third quartiles, respectively.

348 **Fig. 4 | APOE germline variants are associated with survival in humans with SARS-CoV-2**
349 **infection.** **a**, Multivariate analysis of the impact of age, sex, and APOE genotype on survival of patients
350 with SARS-CoV-2 infection in the UK Biobank (P values according to multivariable Cox proportional
351 hazards model, error bars indicate 95% confidence intervals, n = 13,207). **b-d**, Survival of patients from
352 (a) stratified by age below or above median (**b**), sex (**c**), and APOE genotype (**d**). P values in (b-d)
353 according to log-rank tests. n, sample size; HR, hazard ratio for death.

354 **Methods**

355 **Cell Lines**

356 VeroE6 cells (*Chlorocebus sabaeus*; sex: female, kidney epithelial) obtained from the ATCC (CRL-1586)
357 and Ralph Baric (University of North Carolina at Chapel Hill), Caco-2 cells (*H. sapiens*, sex: male, colon
358 epithelial) obtained from the ATCC (HTB-37), and Huh-7.5 hepatoma cells (*Homo sapiens*; sex: male,
359 liver epithelial)⁴³ were cultured in Dulbecco's Modified Eagle Medium (DMEM) supplemented with 1 %
360 nonessential amino acids (NEAA) and 10 % fetal bovine serum (FBS) at 37°C and 5 % CO₂. All cell lines
361 were tested negative for contamination with mycoplasma.

362 **Virus propagation and titration**

363 The SARS-CoV-2 MA10 was generously provided by Ralph Baric (University of North Carolina at Chapel
364 Hill). A P1 stock was amplified in VeroE6 cells obtained from the ATCC that were engineered to stably
365 express TMPRSS2 (VeroE6_{TMPrSS2}). To generate a P2 working stock, VeroE6_{TMPrSS2} cells were infected
366 at a multiplicity of infection (MOI) of 0.1 plaque forming units (PFU)/cell and incubated at 37°C for four
367 days. The virus-containing supernatant was subsequently harvested, clarified by centrifugation (3,000 g
368 for 10 min), and filtered using a disposable vacuum filter system with a 0.22 µm membrane. Virus stock
369 titers were measured by a standard plaque assay (PA) on Huh-7.5 cells that stably express ACE2 and
370 TMPRSS2 (Huh-7.5_{ACE2/TMPRSS2}) and on VeroE6 cells obtained from Ralph Baric (referred to as
371 VeroE6_{UNC}). Briefly, 500 µL of serial 10-fold virus dilutions in Opti-MEM were used to infect 4×10⁵ cells
372 seeded the day prior into wells of a 6-well plate. After 90 min adsorption, the virus inoculum was
373 removed, and cells were overlaid with DMEM containing 10 % FBS with 1.2 % microcrystalline cellulose
374 (Avicel). Cells were incubated for four days at 33°C, followed by fixation with 7 % formaldehyde and
375 crystal violet staining for plaque enumeration. SARS-CoV-2, strain USA-WA1/2020, was obtained from
376 BEI Resources and amplified in Caco-2 cells. Caco-2 cells were infected at a MOI = 0.05 PFU/cell and
377 incubated for 6 days at 37°C. The virus-containing supernatant was subsequently harvested, clarified by

378 centrifugation (3,000 g × 10 min) and stored at -80°C. Viral titers were measured on Huh-7.5 cells by
379 standard plaque assay as described above. All SARS-CoV-2 and SARS-CoV-2 MA10 experiments were
380 performed in a biosafety level 3 (BSL-3) laboratory.

381 To confirm virus identity and evaluate for unwanted mutations that were acquired during the amplification
382 process, RNA from virus stocks was purified using TRIzol Reagent (ThermoFisher Scientific, #15596026).
383 In brief, 200 µL of each virus stock was added to 800 µL TRIzol Reagent, followed by 200 µL chloroform,
384 which was then centrifuged at 12,000 g for 5 min. The upper aqueous phase was transferred to a new
385 tube, mixed with an equal volume of isopropanol, and then added to RNeasy Mini Kit columns (Qiagen,
386 #74014) to be further purified following the manufacturer's instructions. Viral stocks were subsequently
387 confirmed via next generation sequencing using libraries for Illumina MiSeq.

388 **Animal studies**

389 All animal experiments were conducted in accordance with a protocol approved by the Institutional Animal
390 Care and Use Committee at The Rockefeller University, including the use of SARS-CoV-2 MA10 virus
391 under BSL-3 conditions. Human *APOE2* (strain #1547), *APOE3* (#1548), and *APOE4* (#1549) targeted
392 replacement (knock-in) mice on C57Bl/6 background were obtained from Taconic Biosciences.

393 **SARS-CoV-2 MA10 in vivo infections**

394 All infection experiments were performed in a dedicated BSL-3 facility at The Rockefeller University at
395 negative pressure. Staff performing experiments were protected by wearing Tyvek suits connected to
396 powered air purifying respirators. Mice were intranasally infected with 14,700 PFU (based on titration in
397 VeroE6_{UNC} cells) of SARS-CoV-2 MA10 in a volume of 30 µL under ketamine/xylazine anesthesia. *APOE*
398 knock-in mice were infected between 7 and 45 weeks of age as indicated in the figures. Experimental
399 cohorts were age matched. Mice were monitored daily for weight loss and general condition. Mice were
400 recorded as dead when found dead in the cage or when meeting criteria for euthanasia as defined in the
401 animal protocol, including when falling below 70 % initial body weight. All infected mice were included in
402 survival and weight analyses. Some mice were selected before infection for tissue harvest on the days as
403 indicated in the figure legends and censored for survival and weight analyses on the respective days.
404 Mice were gently twirled before weighing to prevent measurement inaccuracies due to mouse
405 movements. In addition, weight measurements were performed with investigators blinded for the
406 genotype in two independent experiments which recapitulated the results of the overall large cohort.

407 **RNA isolation from homogenized lungs**

408 The right lung lobe was resected and homogenized in TRIzol (ThermoFisher Scientific, #15596026) in a
409 gentleMACS dissociator (Miltenyi) according to the manufacturer's instructions (program RNA_01). Debris
410 was removed by centrifugation (2000g for one minute) and RNA was isolated using the Direct-zol RNA
411 purification kit (Zymo Research, #R2050) including DNase digestion according to the manufacturer's
412 instructions.

413 **TaqMan quantitative real-time PCR**

414 For quantification of SARS-CoV-2 MA10 titers from homogenized lungs, RNA was isolated as described
415 above, reverse-transcribed and quantified using the TaqMan Fast Virus One Step Master Mix
416 (ThermoFisher Scientific, #4444436) on a QuantStudio 5 system running QuantStudio Design & Analysis
417 v1.4.3 (Thermo Fisher Scientific) according to the manufacturer's instructions. Primers for viral
418 nucleocapsid were as recommended in the US Centers for Disease Control and Prevention diagnostic N1
419 assay (IDT, #10006713), and 18S rRNA was used as housekeeping control (Thermo Scientific,
420 #4319413E).

421 **Bulk RNA-sequencing**

422 For preparation of RNA-seq libraries, 250-500 ng of RNA isolated from homogenized lungs as outlined
423 above was used as input for the Quantseq 3' FWD library preparation kit (Lexogen, #015). For cohorts 1-
424 2, age-matched 17-23 weeks old male mice were used. For cohort 3, seven weeks old female mice were
425 used. Libraries were sequenced on an Illumina NovaSeq sequencer (single end, 100 bp read length), and
426 polyA and adapter sequences were trimmed using the BBDuk utility (v38.9; options k=13, ktrim=r,
427 forcetrimleft=11, useshortkmers=t, mink=5, qtrim=t, trimq=10, minlength=20). As genome reference,
428 mouse (assembly GRCm38) and SARS-CoV-2 MA10 (Genbank accession number MT952602²¹)
429 genomes were concatenated and trimmed reads were aligned using STAR aligner (v2.7.8a) with default
430 settings, apart from "--outFilterMismatchNoverLmax 0.1" as recommended by Lexogen (personal
431 communication). STAR was also used for counting reads mapping to genes. Further analysis was
432 performed using R (v4.1.0). Two samples (out of 88 samples total) were removed from analysis because
433 of their identification as outliers based on PCA and/or SARS-CoV-2 MA10 transcript abundance.

434 **Weighted gene co-expression network analysis and pathway analysis**

435 Weighted gene co-expression network analysis (WGCNA)⁴⁴ was employed using the WGCNA R package
436 (v1.70) to identify modules of co-expressed genes. WGCNA identifies clusters of genes whose
437 expression correlates with each other and relates these clusters to traits, such as *APOE* genotype and
438 timepoint relative to infection in our study. The module eigengene represents the first principal component
439 of the expression matrix and can be used to summarize the (weighted average) expression of a module.
440 Gene expression data were subjected to library size normalization and variant stabilizing transformation
441 using DESeq2 (v1.32.0) and the top 30% genes in terms of variance of expression were used as input for
442 WGCNA. To compute the adjacency matrix for a signed co-expression network, a soft threshold power of
443 10 was used. To calculate correlations between traits and module eigengenes, *APOE* genotype was
444 assigned values based on its impact on survival as shown in Fig. 1a, and the timepoint trait was assigned
445 values in terms of days relative to infection. Hub genes were identified as the genes exhibiting the highest
446 connectivity within a given model.

447 To assess enrichment of gene sets listed in the Gene Ontology "biological processes", the clusterProfiler
448 package for R (v4.0.0) was used to perform over-representation analysis based on a hypergeometric
449 model.

450 **Single cell RNA-sequencing**

451 For single cell RNA-sequencing (scRNA-seq) of lung-resident cells, mice were anesthetized, and the
452 pulmonary circulation was flushed with 5-10 mL ice-cold PBS. The right lung lobe was dissociated using
453 the lung dissociation kit (130-095-927, Miltenyi Biotec) with a gentleMACS dissociator according to the
454 manufacturer's instructions (program 37C_m_LDK_1). Cells were strained using a 70 µm filter, washed,
455 pelleted, and red blood cells were lysed by incubation in ACK buffer (A10492, Gibco) for two minutes
456 before neutralization with PBS. Cells were then strained again with a 40 µm filter and processed using the
457 cell fixation (SB1001) and single cell whole transcriptome (SB2001) kits from Parse Biosciences
458 according to the manufacturer's instructions. This scRNA-seq approach is based on combinatorial
459 barcoding, which enabled us to multiplex lungs from a total of 29 mice representing each of the three
460 *APOE* genotypes and conditions in the absence and presence of SARS-CoV-2 MA10 infection
461 (**Extended Data Fig. 5a**). One of the eight resulting sublibraries was sequenced on an Illumina Nextseq
462 500 sequencer and the other seven sublibraries were pooled and sequenced on an Illumina Novaseq
463 sequencer (S2 flowcell) to an average depth of 65,256 reads/cell.

464 For data processing, the ParseBioscience processing pipeline (v0.9.6p) was employed at default settings
465 to align sequencing reads to the GRCm38 mouse genome and to demultiplex samples. In brief, each of
466 the eight sublibraries was first processed individually with the `split-pipe -mode all` command and the
467 output of the eight sublibraries was combined with `split-pipe -mode combine`. Downstream processing
468 was performed using the R package Seurat (v4.0.2) at default settings unless otherwise noted. Cells with
469 fewer than 150 or more than 7,500 detected unique genes, more than 40,000 unique molecular
470 identifiers, or more than 15% mitochondrial reads were excluded from analysis. The resulting gene-cell
471 matrix was normalized and scaled using Seurat's `NormalizeData` and `ScaleData` functions and
472 principal component analysis was performed with Seurat's `RunPCA` function; cells were clustered using
473 the `FindNeighbors` (30 dimensions of reduction) and `FindClusters` (resolution = 1.4) functions; for
474 visualizing clusters, `RunUMAP` (30 dimensions) was run. Wilcoxon rank-sum tests were performed to
475 determine differentially expressed genes between clusters using the `FindAllMarkers` function (minimal
476 fraction of 25% and log-transformed fold change threshold of 0.25). The identity of cell clusters was
477 determined by cross-referencing top differentially expressed transcripts with previous studies reporting on
478 single cell transcriptomes of the lung⁴⁵⁻⁴⁷. Ambiguous cells with expression of distinct lineage markers
479 were deemed to be likely multiplets and were excluded. Three clusters expressing T cell markers were
480 characterized further using Seurat's `subset` function and reanalyzed similarly to the main dataset,
481 including running the `RunPCA`, `FindNeighbors` (20 dimensions), `FindClusters` (resolution = 0.5) and
482 `RunUMAP` functions. Ambiguous cells from the subset were removed, and annotations for the remaining
483 clusters were added to the main dataset. For summary analyses, clusters were grouped as follows:
484 Alveolar mØ A and B and proliferating alveolar mØ as alveolar macrophages; monocytes A and B as
485 monocytes; T cells naïve, T cells and T cells proliferating as T cells; myofibroblasts, lipofibroblasts, and
486 *Col14a1*⁺ fibroblasts as fibroblasts; capillary ECs, vascular ECs A and B, other ECs, and *Vcam1*⁺ ECs A

487 and B as endothelial cells; AT1, AT2, ciliated cells, airway epithelial A and B, and mesothelial cells as
488 epithelial cells. In total, filtering low quality and ambiguous cells resulted in 41,500 cells for analysis (of
489 50,104 cells before filtering).

490 For gene set enrichment analysis (GSEA) of the samples from infected mice, differentially expressed
491 genes between either *APOE2* and *APOE3* or *APOE4* and *APOE3* were calculated according to Wilcoxon
492 rank-sum tests using Seurat's `FindMarkers` function. Genes were ranked using the metric $[-\log_{10}(P$
493 $value)]/\text{sign of log-fold change}$. The ranked gene lists were used as input for the `GSEA` function of the
494 clusterProfiler R package (v4.0.0) to assess enrichment of selected immune-related pathways of the
495 Hallmark gene set of the MSigDB database (<http://www.gsea-msigdb.org>).

496 **Histological analysis and immunofluorescence staining**

497 The left lung lobe was resected and fixed by submersion in 4% paraformaldehyde for 24 hours at room
498 temperature. Fixed lungs were embedded in paraffin and sectioned in 5 μm thick slices. Sections were
499 dewaxed and rehydrated by incubation with xylene and descending ethanol concentrations and then
500 either stained with hematoxylin/eosin for histological analysis or processed for immunofluorescence
501 staining.

502 For immunofluorescence staining, samples were permeabilized with 0.1% Triton-X for 15 min. Antigen
503 retrieval was performed by microwaving samples in Tris-EDTA buffer (Abcam, #ab93684) for 20 minutes.
504 Samples were blocked by incubation with 5 % goat serum in PBST (PBS with 0.1 % Tween-20) for one
505 hour. Subsequently, sections were stained with anti-CD45 (polyclonal, Abcam, #ab10558; 1:750) or anti-
506 SARS Nucleocapsid (polyclonal, Novus Biologicals, #56576, 1:1000) at 4°C overnight. All antibodies were
507 diluted in PBST with 5% goat serum. Slides were washed three times with PBS and stained with AF555-
508 conjugated anti-rabbit antibody (1:200 in PBST, ThermoFisher Scientific) for 45 minutes. Slides were
509 washed with PBS and nuclei were counterstained with DAPI (1 $\mu\text{g}/\text{ml}$, Roche) before mounting with
510 Prolong Gold (ThermoFisher Scientific). Images of lung sections were acquired using a Nikon A1R
511 confocal microscope at 20 \times magnification using Nikon NIS elements software (v5.20.02). Images were
512 quantified using CellProfiler (v4.2.1). Three to four randomly sampled fields of view per lung were
513 analyzed and averaged.

514 For histological analysis, H&E-stained lung sections were evaluated and scored by a board-certified
515 veterinary pathologist (S.E.C) using a semiquantitative histopathology scoring system used in mouse
516 models of SARS-CoV-2^{48,49}. Briefly, five random fields of the lung lobe at 200 \times total magnification were
517 chosen and scored in a blinded manner for histopathological changes. Ordinal scores for lesion
518 parameters were assigned using the following tiers: 0 - within expected limits; 1 - uncommon, < 5%; 2 -
519 detectable in 5–33%; 3 - detectable in 34–66% and 4 - detectable in > 66% of lung fields. Tissues were
520 graded for the presence of edema, hemorrhage, fibrin, and/or necrotic debris in alveoli, bronchiolar
521 epithelial necrosis, perivascular and interstitial inflammation, and mononuclear cell infiltrates. Endothelial
522 inflammation (endothelialitis) was evaluated by the extent of the lesion using the following ordinal scoring:

523 0 – absent; 1 - minor, solitary to loose adhesion or aggregation of leukocytes to the vascular endothelium
524 with or without infiltration of leukocytes in the vascular wall / up to five blood vessels affected; 2 –
525 moderate, small to medium adhesion/aggregates and infiltration / six to ten blood vessels affected; and 3
526 – severe, robust leukocytic aggregates and infiltrates around pulmonary vessels / more than ten blood
527 vessels affected. For scoring neutrophil cell infiltration (200-600× objective magnification): 0 - within
528 normal limits; 1 - scattered neutrophils sequestered in septa and/or infiltrating blood vessels; 2 - #1 plus
529 solitary neutrophils extravasated in alveolar spaces; 3 - #2 plus small aggregates in blood vessels,
530 alveolar spaces, and perivascular and peribronchiolar interstitium. An Olympus BX45 light microscope
531 was used to capture images with a DP26 camera using cellSens Dimension software (v1.16). Lungs in
532 SARS-CoV-2 MA10-infected mice exhibited multifocal areas of airway epithelial damage in bronchioles.
533 Bronchioles had focal to multifocal changes characterized by segmental attenuation of bronchiolar
534 epithelium with an accumulation of necrotic cellular debris, fibrin, and sloughed epithelial cells, and
535 occasional foamy macrophages in the airway lumens (**Fig. 2f**). Peribronchiolar interstitium was
536 multifocally infiltrated by increased numbers of neutrophils and lymphocytes. The adjacent alveolar sacs
537 and septae exhibited multifocal to coalescing areas of alveolar damage. Histological changes included
538 hypercellular thickening of the alveolar septae caused by infiltrating leukocytes and congestion of alveolar
539 capillaries, pneumocyte degeneration and necrosis, edema, fibrin strands and increased numbers of
540 macrophages and scattered neutrophils and lymphocytes in alveolar spaces. Often, the vascular
541 endothelium of pulmonary vessels was reactive with adherence and aggregation of leukocytes to the
542 endothelium and transmigrating within vessel walls, indicative of endothelialitis.

543 **Flow cytometry**

544 All steps were performed on ice and under protection from light unless stated otherwise. Peripheral blood
545 was obtained by submandibular bleedings and red blood cells were lysed by incubation in ACK buffer
546 (A10492, Gibco) for three minutes at room temperature before addition of PBS for neutralization. For flow
547 cytometry of dissociated lungs, mice were anesthetized, and the pulmonary circulation was flushed with
548 5-10 mL ice-cold PBS. The right lung lobe was then dissociated using the lung dissociation kit (130-095-
549 927, Miltenyi Biotec) with a gentleMACS dissociator according to manufacturer's instructions (program
550 37C_m_LDK_1). Cells were strained through a 70 µm filter, washed, pelleted and red blood cells were
551 lysed by incubation in ACK buffer as indicated above before addition of PBS for neutralization. Cells were
552 pelleted by centrifugation at 200×g for 5 minutes and resuspended in staining buffer (25 mM HEPES, 2 %
553 FBS, 10 mM EDTA (351-027, Quality Biological), and 0.1 % sodium azide (7144.8-16, Ricca) in PBS). To
554 block Fc receptors, cells were incubated with 2.5 µg/mL anti-CD16/32 antibody in staining buffer (clone
555 93; 101320, BioLegend) before incubation with antibodies diluted in staining buffer for 20 minutes. After
556 washing with PBS, cells were incubated with Zombie NIR Fixable Live/Dead stain (423105, BioLegend;
557 1:10,000 in PBS) for 15 minutes at room temperature, washed with staining buffer, and fixed in 4% PFA.
558 CountBright counting beads (C36950, Thermo Fisher) were added to the peripheral blood samples before
559 analysis on an LSR Fortessa (BD Biosciences). For compensation, single color controls with UltraComp

560 beads (01-2222-42, ThermoFisher) for antibodies and amine-reactive beads (A10628, ThermoFisher) for
561 Zombie live-dead stain were used. The following anti-mouse fluorophore-conjugated antibodies were
562 used: CD45-BV785 (clone: 30-F11, cat#: 103149, supplier: BioLegend, dilution: 1:3,000), CD11b-FITC
563 (M1/70, 101206, BioLegend, 1:1,000), Ly6G-PerCP/Cy5.5 (1A8, 127616, BioLegend, 1:1,000), Ly6C-
564 BV711 (HK1.4, 128037, BioLegend, 1:10,000), I-A/I-E-PE (M5/114.15.2, 107607, BioLegend, 1:10,000),
565 CD19-PB (6D5, 115526, BioLegend, 1:500), CD19-BV421 (6D5, 115549, BioLegend, 1:500), NK1.1-APC
566 (PK136, 17-5941-82, eBiosciences, 1:500), CD4-BV605 (GK1.5, 100451, BioLegend, 1:300), CD8 α -
567 AF700 (53-6.7, 100730, BioLegend, 1:1,000). For staining of SARS-CoV-2 spike-specific CD8 $^+$ T cells,
568 BV421-labeled SARS-CoV-2 S 539-546 tetramer was used (NIH Tetramer Core Facility, 1:200).

569 **SARS-CoV-2 in vitro infections**

570 The day prior to infection, Huh-7.5 cells were seeded into 96-well plates at a density of 7.5×10^3 cells/well.
571 The next day, recombinant APOE2, -3, -4 (21-9195, 21-9189, 21-9190, Tonbo Biosciences) or BSA
572 (A9576, Sigma) as control were added to the wells at a concentration of 10 $\mu\text{g}/\text{mL}$, followed by infection
573 with SARS-CoV-2 (WA1/2020) at an MOI of 0.01 PFU/cell. Cells were then incubated at 33°C for 48 h.
574 Next, they were fixed by adding an equal volume of 7% formaldehyde to the wells and subsequently
575 permeabilized with 0.1% Triton X-100 for 10 min. After extensive washing, SARS-CoV-2 infected cells
576 were incubated for one hour at room temperature with blocking solution of 5% goat serum in PBS (005-
577 000-121, Jackson ImmunoResearch). A rabbit polyclonal anti-SARS-CoV-2 nucleocapsid antibody
578 (GTX135357, GeneTex) was added to the cells at 1:1,000 dilution in blocking solution and incubated at
579 4°C overnight. A goat anti-rabbit AlexaFluor 594 (A-11012, Life Technologies) was used as a secondary
580 antibody at a 1:2,000 dilution. Nuclei were stained with Hoechst 33342 (62249, Thermo Scientific) at a 1
581 $\mu\text{g}/\text{mL}$ dilution. Images were acquired with a fluorescence microscope and analyzed using ImageXpress
582 Micro XLS (Molecular Devices, Sunnyvale, CA). All SARS-CoV-2 experiments were performed in a
583 biosafety level 3 laboratory.

584 **Analysis of the UK Biobank**

585 *APOE* genotyping results as determined by the rs7412 and rs429358 single nucleotide polymorphisms
586 were downloaded from the UK Biobank⁵⁰. Clinical data, including SARS-CoV-2 test results and survival
587 data were downloaded from the UK Biobank data portal on June 22, 2021. For survival analyses, in
588 patients with multiple tests the earliest positive test result was used as day zero of infection and COVID-
589 19-associated death was recorded if the death cause was ICD10-coded as U07.1 or U07.2. Out of
590 502,619 patients, *APOE* genotype could be determined in 413,219 patients. 77,221 participants had
591 SARS-CoV-2 test results available, and 16,562 patients of these were tested positive at least once
592 (**Extended Data Fig. 7a**). *APOE2/APOE4* heterozygous patients ($n = 10,456$) were excluded from
593 analyses except for summary statistics shown in Extended Data Fig. 7a. For visualization purposes,
594 survival data were truncated at 40 days. To account for genetic ancestry, the first ten genetic principal
595 components as provided by the UK Biobank were included in a multivariate analysis. To restrict the
596 analyses to individuals of European genetic ancestry, field 22006 provided by UK Biobank was used.

597 **Statistical analysis**

598 R v 4.1.0 was used for data visualization and analyses. Statistical tests and sample sizes are listed in the
599 respective figure legends. Unless otherwise noted, data are expressed as mean \pm standard error of the
600 mean. For boxplots, hinges represent the first and third quartiles, whiskers extend to the smallest and
601 largest value within $1.5 \times$ interquartile ranges of the hinges, and points represent individual mice. Survival
602 analyses were performed using the R packages 'survival' and 'survminer'; summary tables were compiled
603 using the 'gtsummary' package. Multivariate analyses were performed according to a Cox proportional
604 hazards model using the 'survival' package and visualized with the 'forestmodel' package. A significant
605 difference was concluded at $P < 0.05$ in all figures.

606 **Data availability**

607 Bulk RNA-seq and scRNA-seq data have been deposited at the Gene Expression Omnibus (GEO) under
608 accession numbers GSE184289 and GSE199498, respectively. All data from the UK Biobank is publicly
609 available under www.ukbiobank.ac.uk. MSigDB is publicly available under <http://www.gsea-msigdb.org>.
610 Source data is provided with this paper.

611 **Code availability**

612 Code is publicly available at https://github.com/benostendorf/ostendorf_etal_2022.

613 **Methods-related references**

- 614 43. Blight, K. J., McKeating, J. A. & Rice, C. M. Highly Permissive Cell Lines for Subgenomic and Genomic Hepatitis C Virus RNA
615 Replication. *Journal of Virology* **76**, 13001–13014 (2002).
- 616 44. Zhang, B. & Horvath, S. A General Framework for Weighted Gene Co-Expression Network Analysis. *Statistical Applications in*
617 *Genetics and Molecular Biology* **4**, (2005).
- 618 45. Angelidis, I. *et al.* An atlas of the aging lung mapped by single cell transcriptomics and deep tissue proteomics. *Nat Commun*
619 **10**, 963 (2019).
- 620 46. Hurskainen, M. *et al.* Single cell transcriptomic analysis of murine lung development on hyperoxia-induced damage. *Nat*
621 *Commun* **12**, 1565 (2021).
- 622 47. Melms, J. C. *et al.* A molecular single-cell lung atlas of lethal COVID-19. *Nature* **595**, 114–119 (2021).
- 623 48. Zheng, J. *et al.* COVID-19 treatments and pathogenesis including anosmia in K18-hACE2 mice. *Nature* **589**, 603–607 (2021).
- 624 49. Sun, J. *et al.* Generation of a Broadly Useful Model for COVID-19 Pathogenesis, Vaccination, and Treatment. *Cell*
625 S0092867420307418 (2020) doi:10.1016/j.cell.2020.06.010.
- 626 50. Bycroft, C. *et al.* The UK Biobank resource with deep phenotyping and genomic data. *Nature* **562**, 203–209 (2018).

627 **Acknowledgments**

628 We are grateful to members of the Tavazoie laboratory and to Daniel Mucida for comments on previous
629 versions of the manuscript. We thank Rockefeller University resource centers for assistance: Vaughn
630 Francis and other veterinary staff of the Comparative Bioscience Center for animal husbandry and care,
631 Connie Zhao, Christine Lai and staff at the genomics resource center for assistance with RNA-seq, and
632 Gaitree McNab for advice on biosafety measures. We thank the Laboratory of Comparative Pathology for
633 histopathology support (with funding from NIH Core Grant P30 CA008748), the group of Ralph Baric for

634 generating the mouse adapted SARS-CoV-2 MA10 strain and making it available to the scientific
635 community, and Rachel Yamin for experimental advice. We thank the NIH Tetramer Core Facility for
636 providing BV421-labeled SARS-CoV-2 S 539-546 tetramer [H-2K(b)]. This work was supported by the
637 Pershing Square Innovation Fund. B.N.O. was supported by a Max Eder grant of the German Cancer Aid
638 (reference 70114327), the David Rockefeller Graduate program in Bioscience, and is a fellow of the
639 digital clinician scientist program at BIH-Charité. J.B. was supported by a scholarship from the German
640 National Academic Foundation. M.A.P. was supported in part by the National Center for Advancing
641 Translational Sciences, NIH, through Rockefeller University, Grant UL1 TR001866. S.F.T. was supported
642 by the Black Family Foundation, The Rockefeller Center for Human Metastasis Research, and The Breast
643 Cancer Research Foundation. C.M.R. was supported by the G. Harold and Leila Y. Mathers Charitable
644 Foundation, the Bawd Foundation, and Fast Grants, a part of Emergent Ventures at the Mercatus Center,
645 George Mason University. Human data analyses were conducted using the UK Biobank Resource under
646 Application Number 62709.

647 **Author contributions**

648 B.N.O. and S.F.T. conceived the study and wrote the manuscript. B.N.O., C.M.R. and S.F.T. supervised
649 all research. B.N.O., J.B., M.A.P., and H.-H.H. conducted experiments. S.E.C. performed pathological
650 analysis of lung sections. All authors edited and approved the manuscript.

651 **Competing interests**

652 The authors declare no competing financial interests.

653 **Additional information**

654 **Correspondence and requests for materials** should be addressed to B.N.O. or S.F.T.

655 **Extended Data figure legends**

656 **Extended Data Fig. 1 | Expanded characteristics of *APOE* knock-in mice infected with SARS-CoV-2**
657 **MA10. a-c**, Distribution of age at infection (**a**), sex (**b**), and *APOE* genotype (**c**) of *APOE* knock-in mice
658 infected with SARS-CoV-2 MA10 (n = 328; data pooled from 13 independent experiments). **d**, Individual
659 weight course of male and female *APOE* knock-in mice infected with SARS-CoV-2 MA10 from (a). **e-f**,
660 Multivariate analysis of the impact of age, sex, *APOE* genotype, and the interaction of age/*APOE* and
661 sex/*APOE* on survival of SARS-CoV-2 MA10-infected *APOE* knock-in mice from (a) (P values according
662 to multivariable Cox proportional hazards model; error bars in (f) denote 95% confidence intervals; n =
663 128, 82, and 118 for *APOE2*, *APOE3*, and *APOE4*, respectively). **g-h**, Survival of young (< 30 weeks old)
664 (**g**) and old (> 30 weeks old) (**h**) SARS-CoV-2 MA10-infected *APOE*-knock-in mice from (a) stratified by
665 *APOE* genotype; P values according to log-rank tests. **i-k**, Age (**i**), sex distribution (**j**), and survival of non-
666 infected *APOE* knock-in mice over a two-week period (**k**) (n = 67, 55, 67 for *APOE2*, *APOE3*, and
667 *APOE4*, respectively; P values according to Kruskal-Wallis (i) and logrank (k) tests). Boxplot whiskers in

668 (a) extend to the smallest and largest value within $1.5 \times$ interquartile ranges of the hinges, and box centre
669 and hinges indicate median and first and third quartiles, respectively.

670 **Extended Data Fig. 2 | Viral load early post infection and extended histopathologic analysis of**
671 **lungs from SARS-CoV-2 MA10-infected APOE knock-in mice.** **a**, TaqMan qPCR for SARS-CoV-2 N1
672 in homogenized lungs from APOE knock-in mice on day 2 post infection with SARS-CoV-2 MA10 (data
673 pooled from two experiments; P values according to one-tailed Mann-Whitney test; $n = 12, 11, 11$ for
674 APOE2, APOE3, and APOE4, respectively; boxplot whiskers extend to the smallest and largest value
675 within $1.5 \times$ interquartile ranges of the hinges, and box centre and hinges indicate median and first and
676 third quartiles, respectively). **b-h**, Histopathologic scoring of lungs from APOE knock-in mice on day 4
677 post infection with SARS-CoV-2 MA10 for hemorrhage (**b**), edema (**c**), mononuclear cell infiltrates (**d**),
678 neutrophilic cell infiltrates (**e**), interstitial infiltrates (**f**), perivascular infiltrates (**g**), and
679 endothelialitis/vascular changes (**h**); P values according to two-sided Mann Whitney-tests, $n = 18, 22, 15$
680 for APOE2, APOE3, and APOE4, respectively.

681 **Extended Data Fig. 3 | Extended analysis of transcriptional profiles and immune cell infiltration in**
682 **APOE knock-in mice during COVID-19.** **a**, Module eigengenes averaged per condition. **b**, Independent
683 validation of correlation of specific gene modules with APOE genotype in lungs of male APOE knock-in
684 mice on day 4 post infection with SARS-CoV-2 MA10. Red indicates positive correlation of module
685 eigengenes with APOE genotype ordered by its impact on COVID-19 survival ($E3 > E2 > E4$); stars
686 indicate significant correlations (one-sided Pearson correlation tests). **c**, Averaged module eigengenes in
687 the validation experiment. **d**, Correlation of gene modules with APOE genotype in lungs of 7-weeks old
688 female APOE knock-in mice on day 4 post infection. Red indicates positive correlation of module
689 eigengenes with APOE genotype ordered by its impact on COVID-19 survival ($E3 > E2 > E4$); stars
690 indicate significant correlations (one-sided Pearson correlation tests). **e**, Averaged module eigengenes of
691 modules significantly associated with APOE genotype in mice from (d). **f-g**, Network plots of the top ten
692 hubgenes (genes with highest intramodular connectivity) (**f**) and the top five GO pathways enriched in the
693 348 genes of the black module (**g**) (P values according to hypergeometric tests adjusted for FDR). **h**,
694 Expression of genes constituting the midnightblue and greenyellow modules. Hubgenes are annotated by
695 name. **i-o**, Network plots of the top ten hubgenes (**i, k, m, o**) and the top five GO pathways enriched in
696 45, 67, and 58 genes of the greenyellow, midnightblue, and yellow modules, respectively (**j, l, n**) (P
697 values in **j, l, and n** according to hypergeometric tests adjusted for FDR). No pathways were enriched in
698 the 24 genes making up the pink module. **p**, Immunofluorescence staining for CD45⁺ cells in lungs of
699 APOE knock-in mice on day 4 post infection ($n = 10, 15, 10$ for APOE2, APOE3, and APOE4,
700 respectively; P values according to two-sided Mann Whitney tests; boxplot whiskers extend to the
701 smallest and largest value within $1.5 \times$ interquartile ranges of the hinges, and box centre and hinges
702 indicate median and first and third quartiles, respectively). Images on the right show representative
703 sections; scale bar, 100 μm .

704 **Extended Data Fig. 4 | Immune cell profiling of lungs and peripheral blood of *APOE* knock-in mice**
705 **with COVID-19.** **a-b,** Gating strategy to delineate leukocyte subsets (**a**) and assessment of the
706 proportion of leukocyte subsets (**b**) in dissociated lungs of *APOE* knock-in mice on day 4 post infection
707 with SARS-CoV-2 MA10 (n = 21, 15, 20 for *APOE2*, *APOE3*, and *APOE4*, respectively; data pooled from
708 two independent experiments; P values according to one-tailed t-tests). **c,** Gating strategy to delineate
709 leukocyte subsets in peripheral blood of *APOE* knock-in mice with COVID-19. **d-g,** Concentration of
710 CD45⁺ leukocytes (**d**) and proportion of myeloid (**e**) and lymphoid (**f**) subsets in the peripheral blood of
711 *APOE* knock-in mice on day 4 post infection with SARS-CoV-2 MA10 as assessed by flow cytometry (n =
712 10, 9, 7 for *APOE2*, *APOE3*, and *APOE4*, respectively; P values according to two-sided t tests). **g,**
713 Representative flow cytometry plots for (e-f). Boxplot whiskers in b and d-f extend to the smallest and
714 largest value within 1.5 × interquartile ranges of the hinges, and box centre and hinges indicate median
715 and first and third quartiles, respectively.

716 **Extended Data Fig. 5 | Extended single cell RNA-sequencing data.** **a,** Number of samples per
717 genotype and condition for single cell RNA-sequencing (scRNA-seq). **b,** Uniform manifold approximation
718 and projection (UMAP) plot of 41,500 RNA-sequenced cells from *APOE* knock-in mice with or without
719 COVID-19. **c-d,** Heatmaps of manually curated marker genes (**c**) and of top three differentially expressed
720 genes per cluster (**d**) for cells from (b).

721 **Extended Data Fig. 6 | Cellular composition in lungs from *APOE* knock-in mice with or without**
722 **COVID-19.** **a,** Fraction of grouped clusters of RNA-sequenced lung cells in *APOE* knock-in mice with or
723 without COVID-19 (n = 9 and 20 for non-infected and infected, respectively; P values according to two-
724 tailed t tests). **b-c,** Fraction of clusters in immune (**b**) and non-immune (**c**) cells from infected mice from
725 (a) (n = 6, 6, and 8 for *APOE2*, *APOE3*, and *APOE4*, respectively; P values according to two-tailed t
726 tests). Boxplot whiskers in a-c extend to the smallest and largest value within 1.5 × interquartile ranges of
727 the hinges, and box centre and hinges indicate median and first and third quartiles, respectively.

728 **Extended Data Fig. 7 | *APOE* genotyping and SARS-CoV-2 test results in participants of the UK**
729 **Biobank.** **a,** General characteristics of the UK Biobank population. **b,** Distribution of *APOE* genotype in
730 participants of the UK Biobank versus the ARIC study (Blair et al., Neurology, 2015) (P = 0.2, Chi-squared
731 test). **c-e,** Distribution of *APOE* genotype in UK Biobank patients with positive versus negative SARS-
732 CoV-2 test (**c**), with positive test versus negative test or untested (**d**), and with SARS-CoV-2 test
733 performed in- versus outpatient (**e**). Tables in (c-e) show odds ratios for testing positive versus negative,
734 having a positive versus negative or no test, and having at least one inpatient versus only outpatient
735 tests, respectively; P values are based on binomial general linearized models. Numbers on top of bars
736 indicate sample sizes.

737 **Extended Data Fig. 8 | The impact of *APOE* genotype on COVID-19 outcome is not confounded by**
738 **population structure or its impact on longevity.** **a,** Multivariate analysis of the impact of age, sex, the
739 first ten genetic principal components, and *APOE* genotype on survival of patients with SARS-CoV-2

740 infection in the UK Biobank (P values according to multivariable Cox proportional hazards model, n =
741 13,207). **b-c**, Dot plot of the genetic principal components 1-2 (**b**) and 3-4 (**c**) colored by *APOE* genotype
742 of SARS-CoV-2-positive patients of the UK Biobank. PC, principal component. **d-e**, Dot plot of the genetic
743 principal components 1-2 (**d**) and 3-4 (**e**) colored by *APOE* genotype of SARS-CoV-2-positive patients
744 with European ancestry in the UK Biobank. **f**, Multivariate analysis of the impact of age, sex, and *APOE*
745 genotype on survival of patients with European ancestry and SARS-CoV-2 infection in the UK Biobank (P
746 values according to multivariable Cox proportional hazards model, n = 10,333). **g**, Survival of patients
747 from (f) stratified by *APOE* genotype (P value in according to log-rank test). **h**, Survival of UK biobank
748 participants over a 30 day observation period in January 2019. The start of the observation period was
749 Jan 1, 2019, and data were censored on Jan 31, 2019 (P value according to log-rank test; n = 384,106).
750 Error bars in a and f indicate 95% confidence intervals.

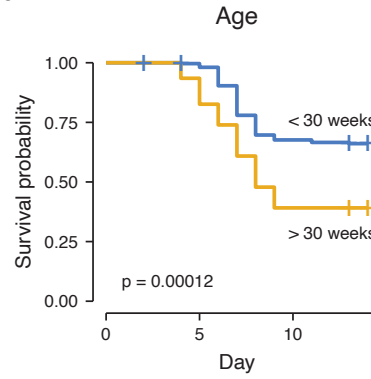
All

a

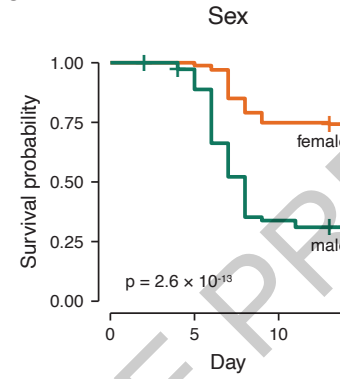
Multivariate analysis

Variable	n	HR	p
Age	328	1.03 (1.01, 1.06)	0.012
Sex			
female	167	Reference	
male	161	5.21 (3.42, 7.93)	1.4e-14
Genotype			
APOE3	82	Reference	
APOE2	128	3.51 (1.56, 7.87)	0.002
APOE4	118	6.54 (2.92, 14.64)	4.9e-06

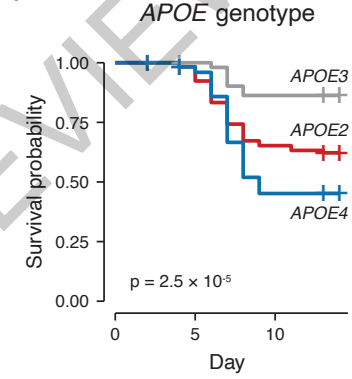
b



c

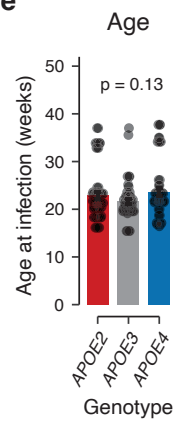


d

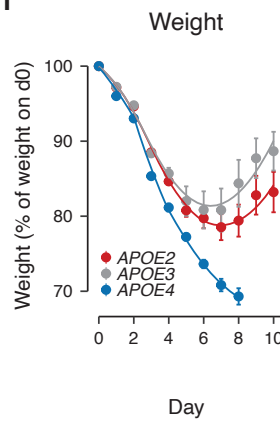


Males

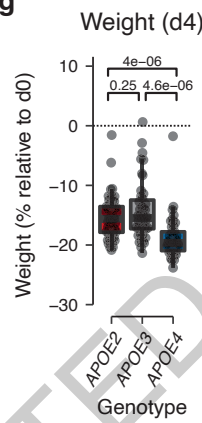
e



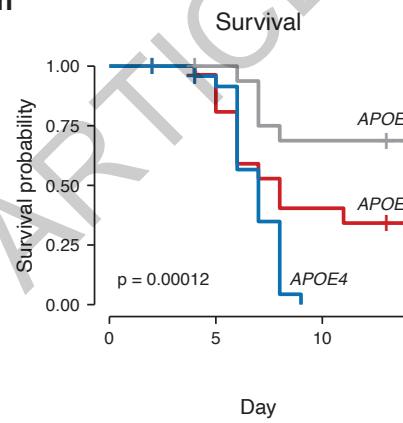
f



g



h

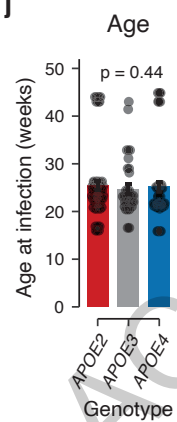


i

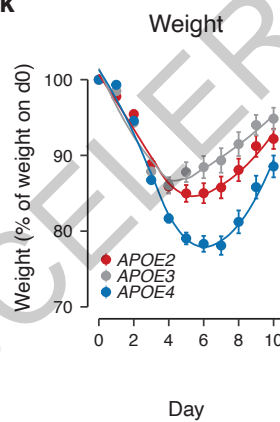
Variable	n	HR	p
Genotype			
APOE3	47	Reference	
APOE2	61	3.24 (1.22, 8.55)	0.02
APOE4	53	6.79 (2.54, 18.18)	1e-04

Females

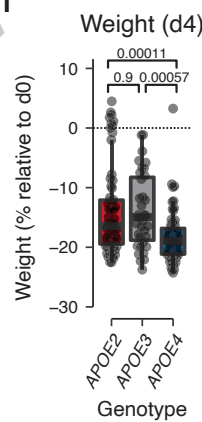
j



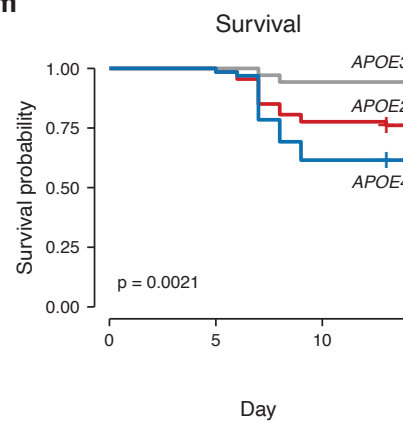
k



l

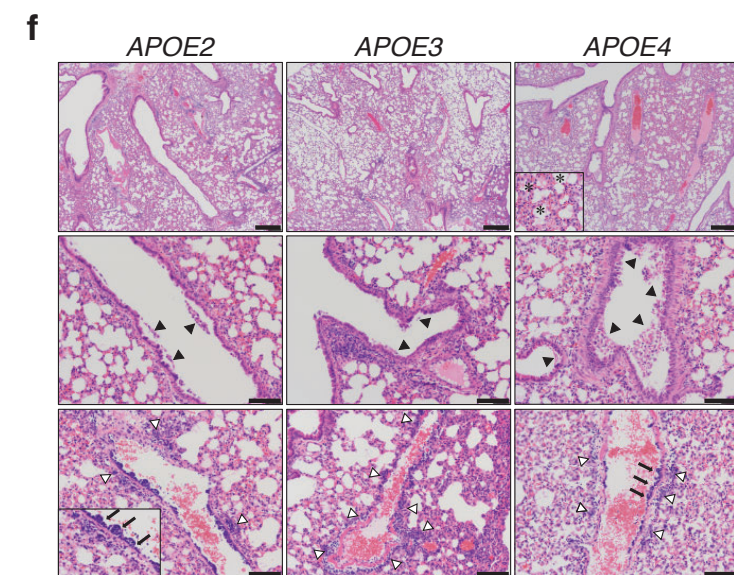
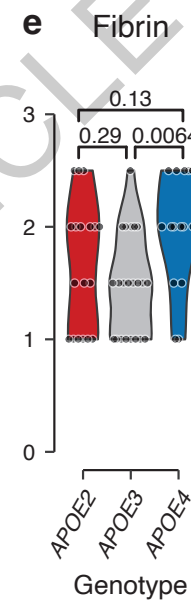
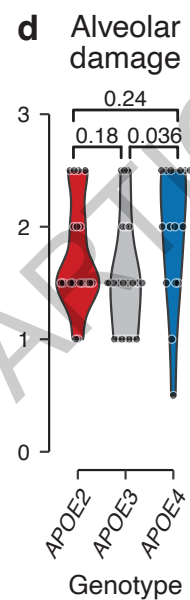
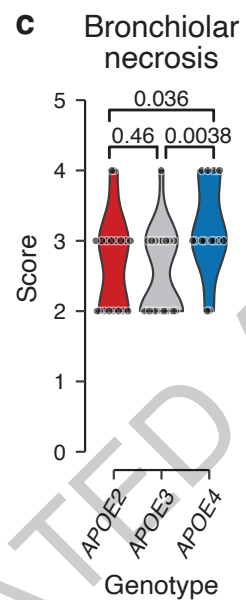
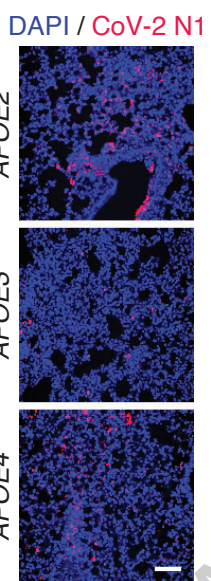
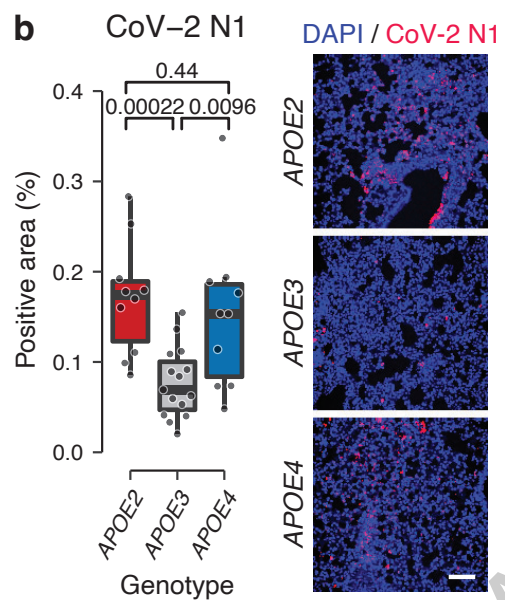
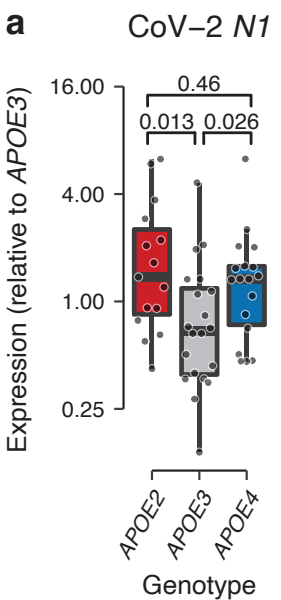


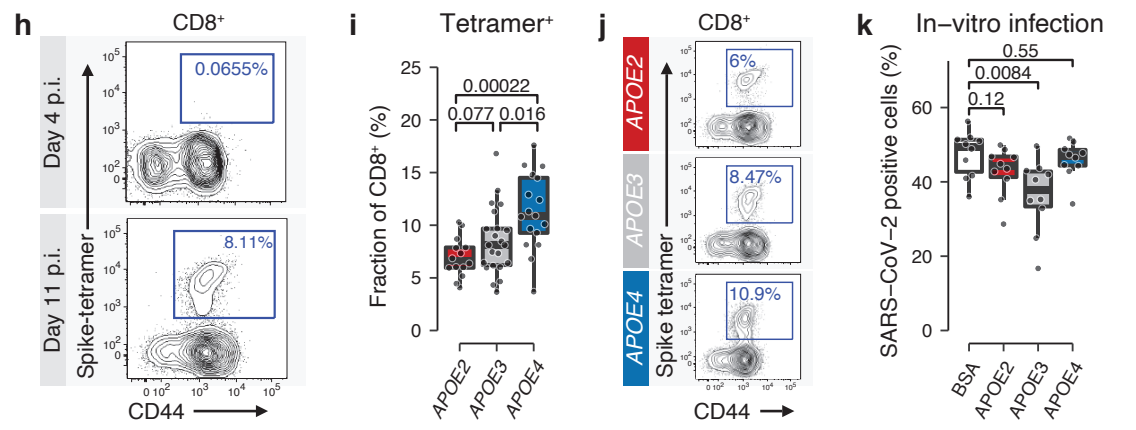
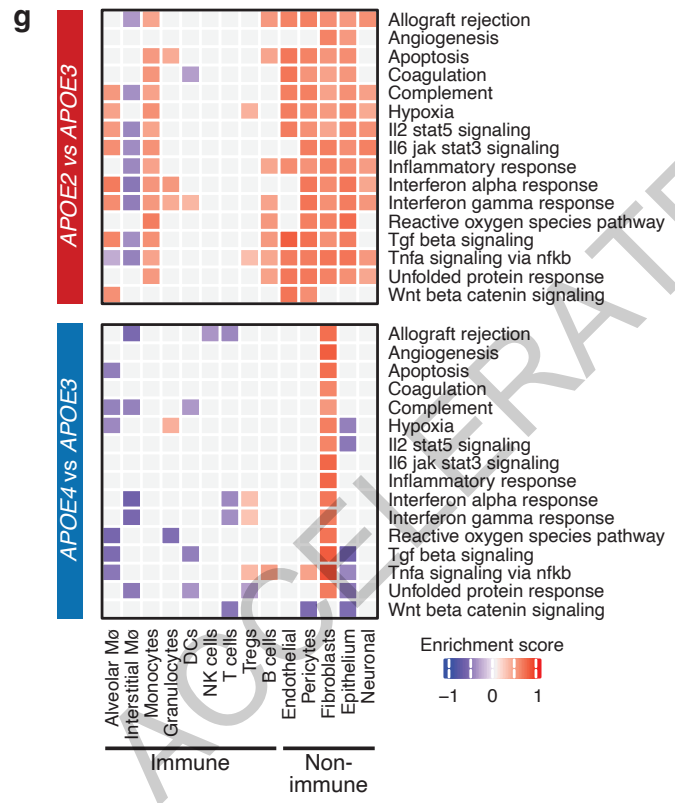
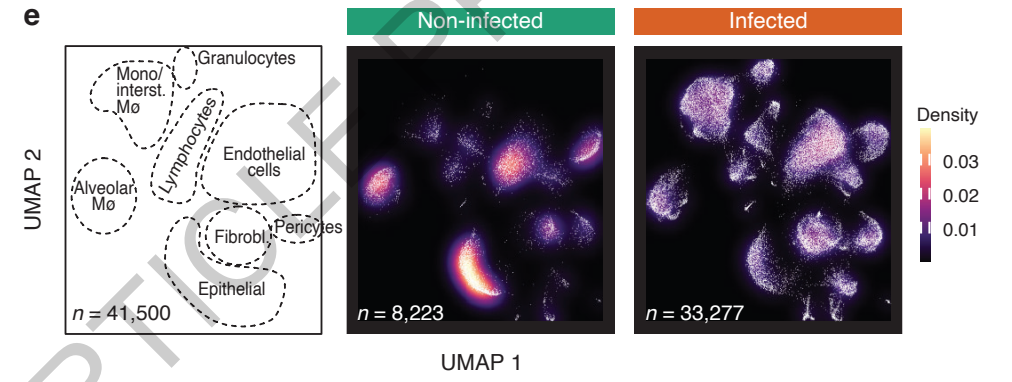
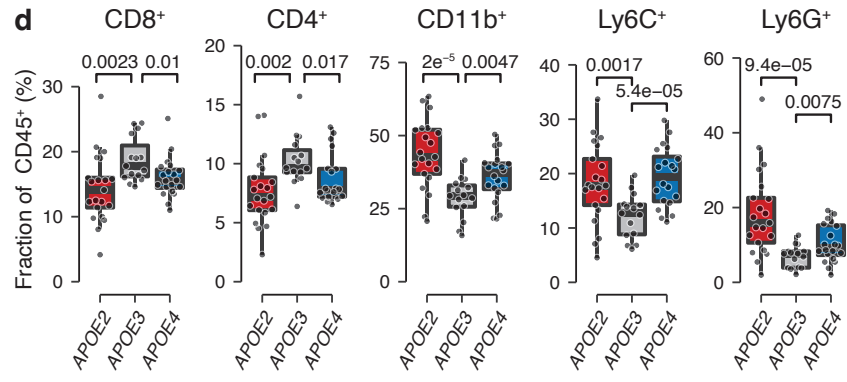
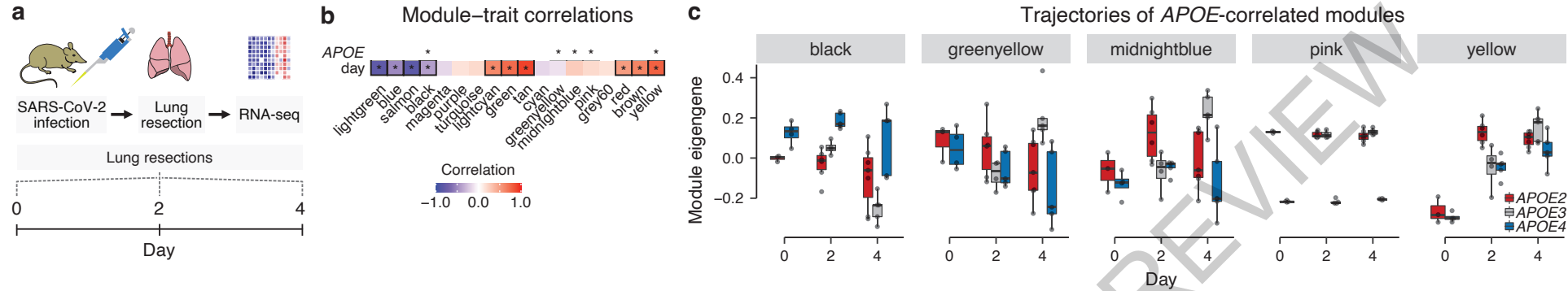
m



n

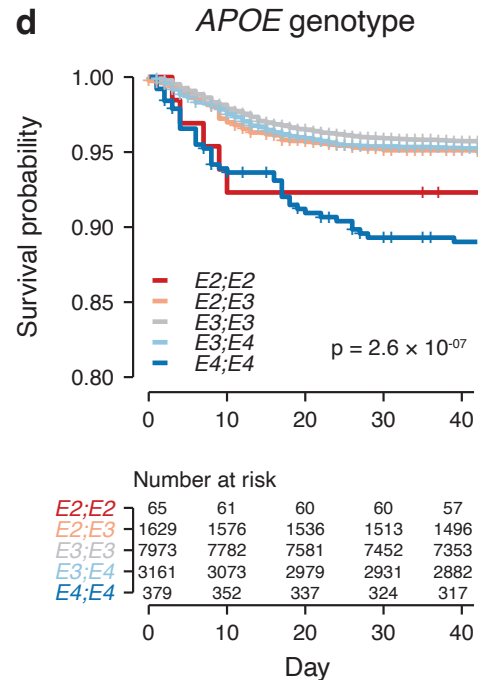
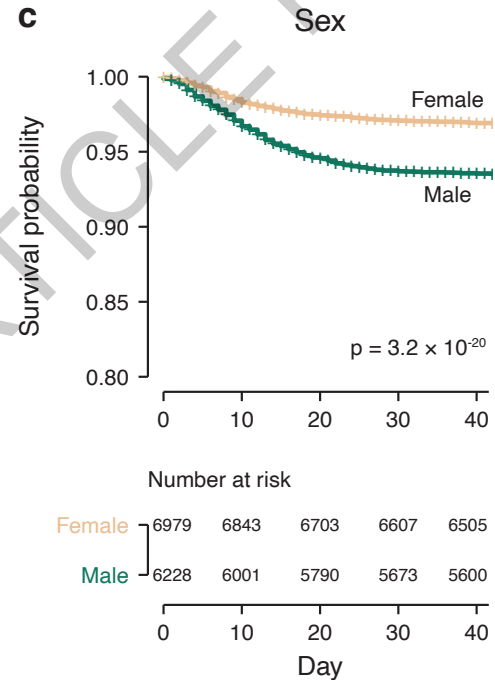
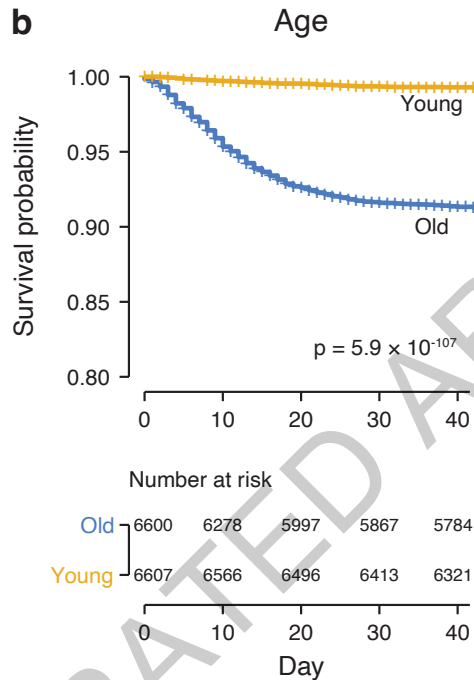
Variable	n	HR	p
Genotype			
APOE3	35	Reference	
APOE2	67	4.67 (1.07, 20.31)	0.040
APOE4	65	8.11 (1.92, 34.23)	0.004

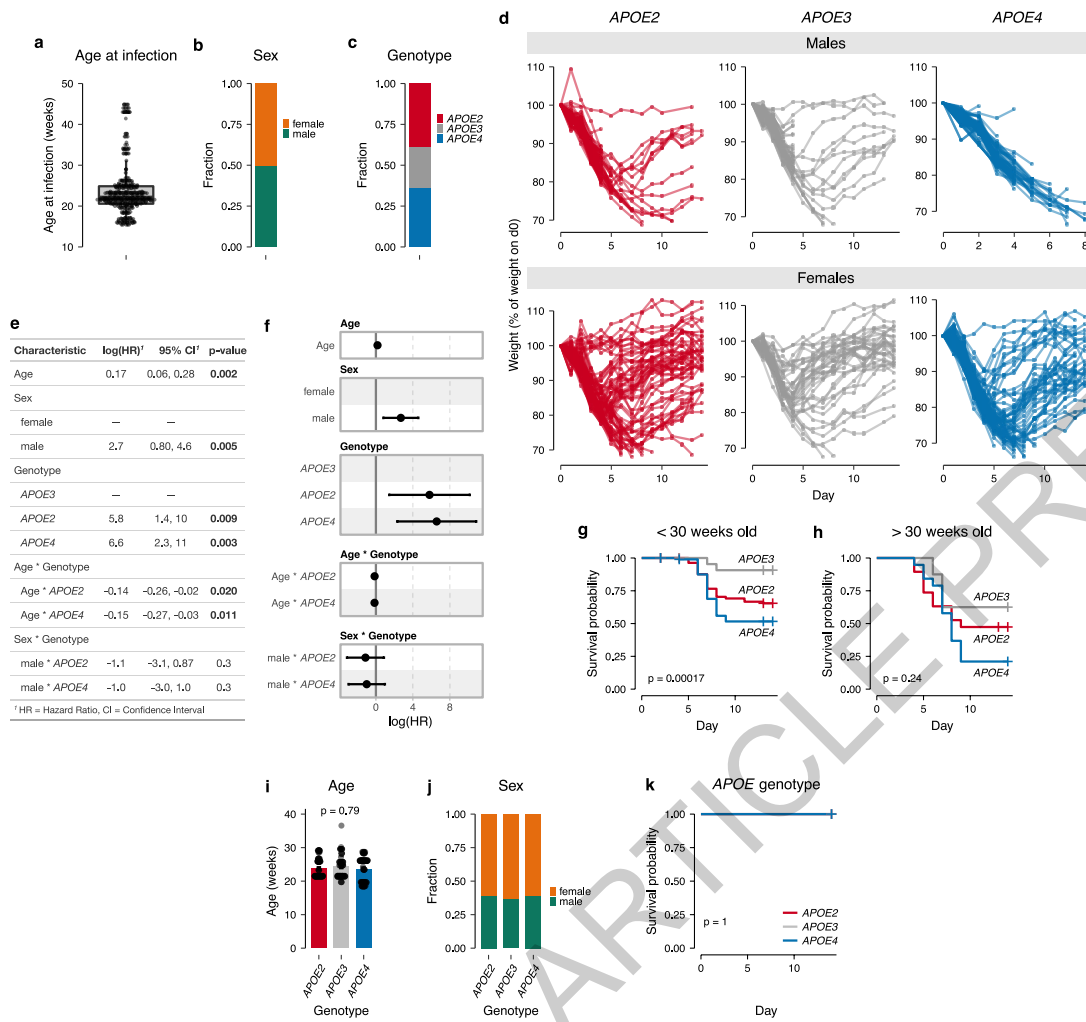




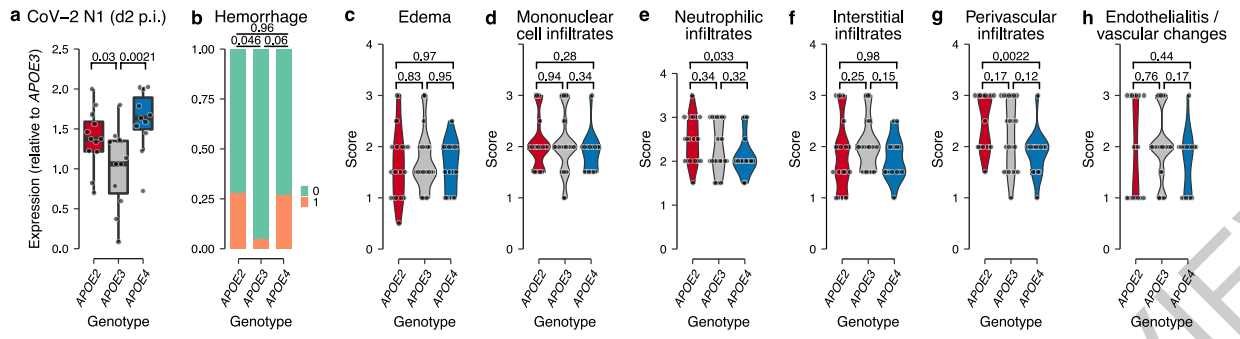
a Multivariate analysis UK Biobank

Variable	n	HR	p
Age	13207	1.16 (1.15, 1.17)	5.9e-122
Sex			
Female	6979	Reference	
Male	6228	1.92 (1.63, 2.26)	5.9e-15
Genotype			
<i>E3</i> ; <i>E3</i>	7973	Reference	
<i>E2</i> ; <i>E2</i>	65	1.64 (0.68, 3.97)	0.3
<i>E2</i> ; <i>E3</i>	1629	1.12 (0.88, 1.42)	0.4
<i>E3</i> ; <i>E4</i>	3161	1.04 (0.86, 1.26)	0.7
<i>E4</i> ; <i>E4</i>	379	2.26 (1.64, 3.13)	7.6e-07



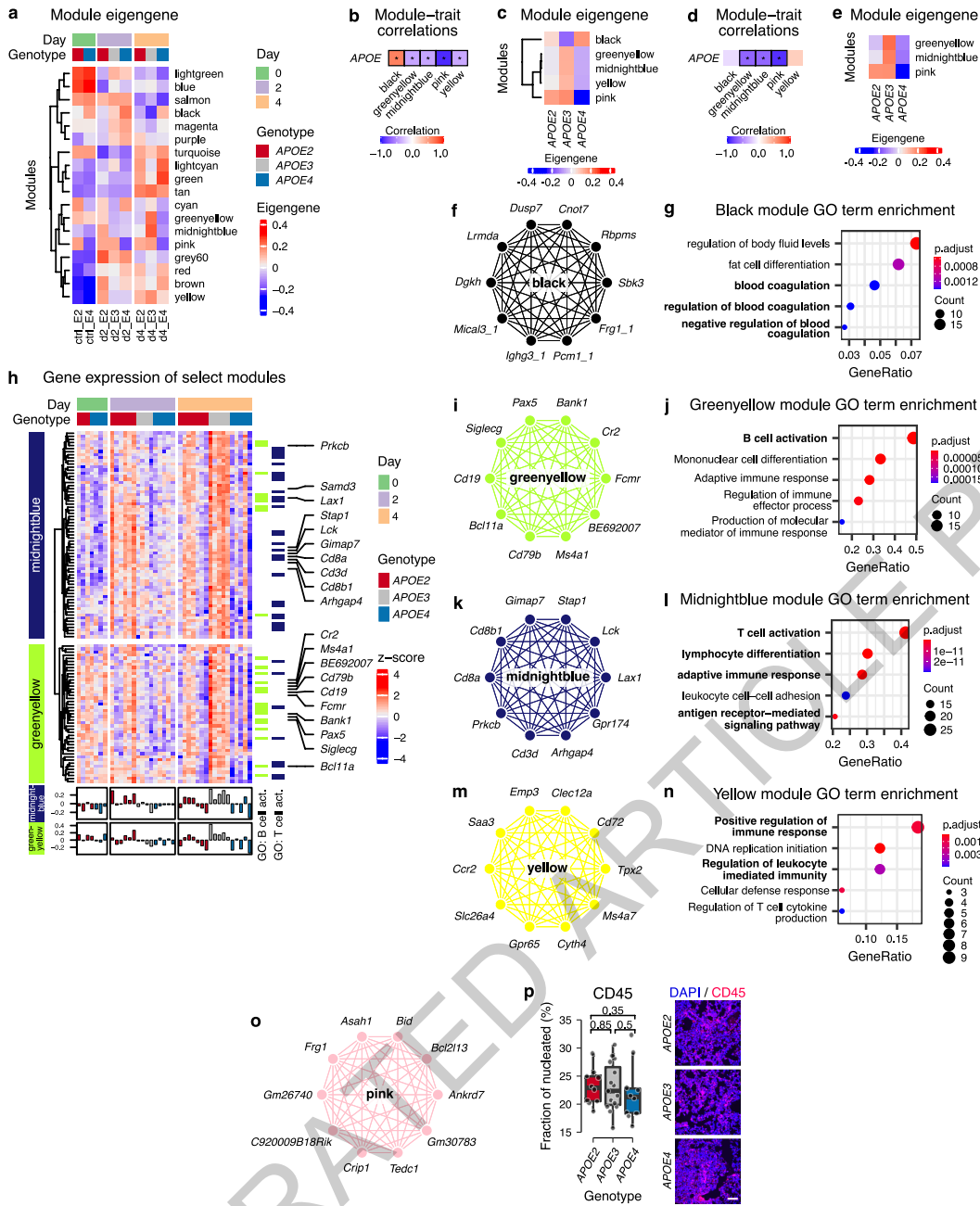


Extended Data Fig. 1

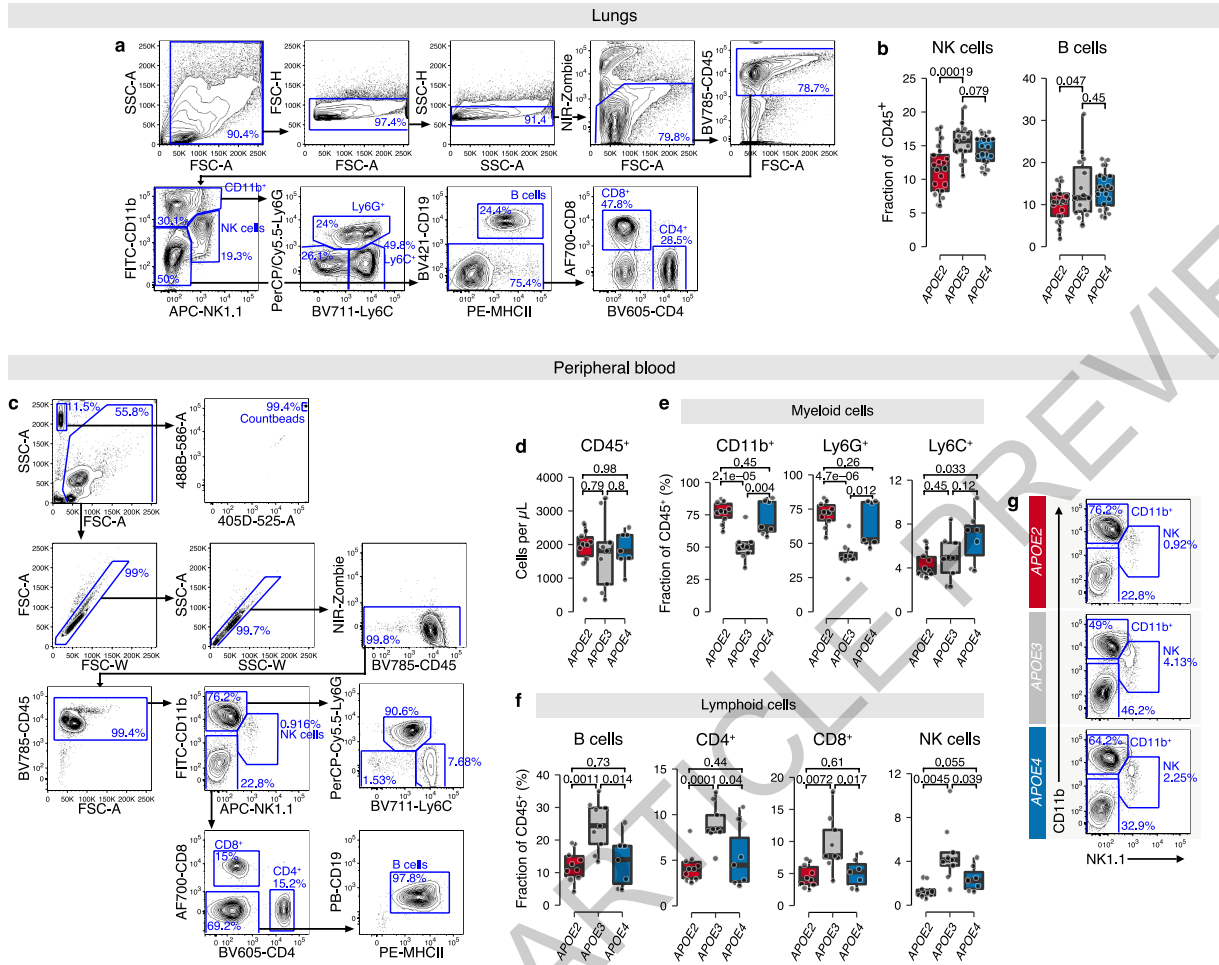


Extended Data Fig. 2

ACCELERATED ARTICLE PREVIEW

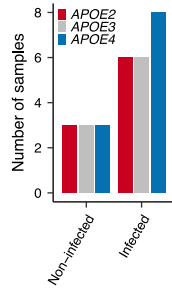


Extended Data Fig. 3

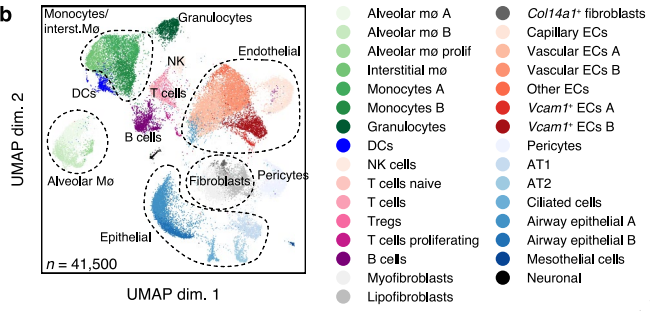


Extended Data Fig. 4

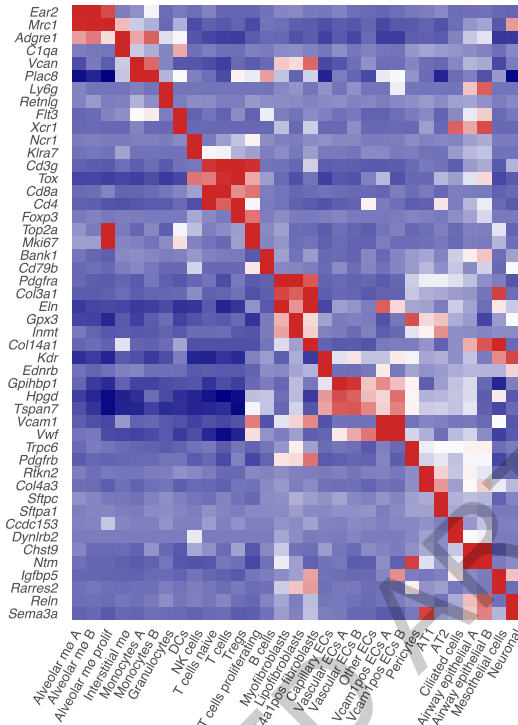
a Samples scRNA-seq



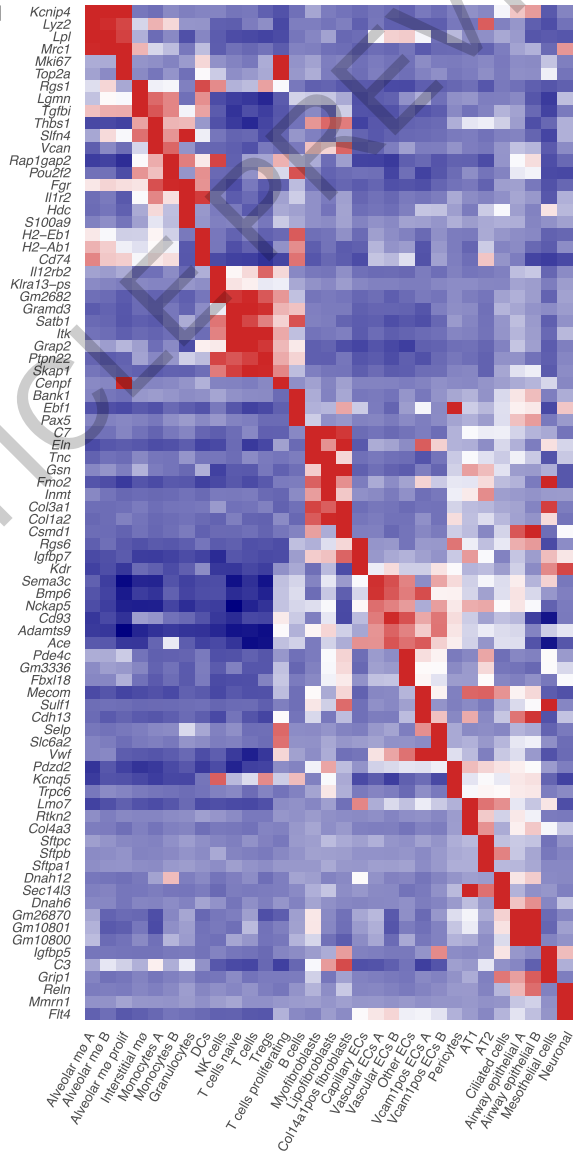
b



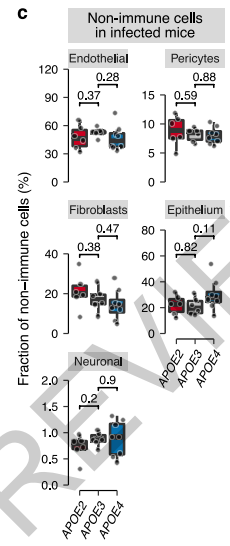
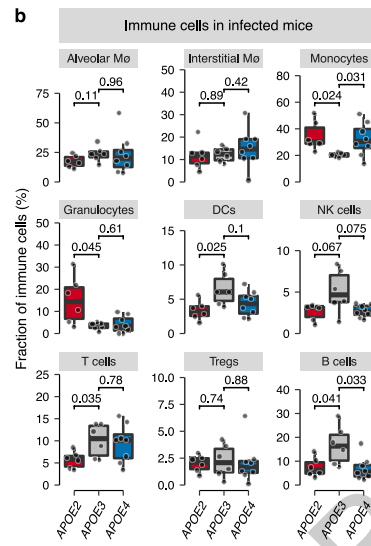
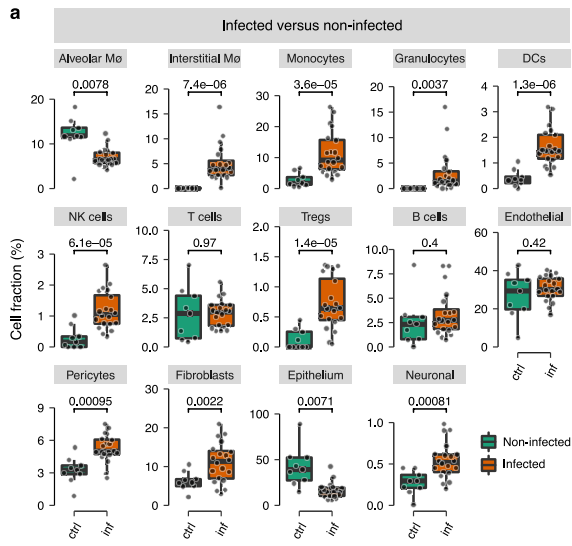
c



d



Extended Data Fig. 5



Extended Data Fig. 6

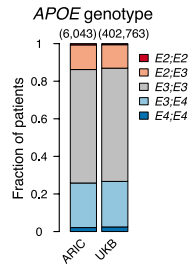
ACCELERATED ARTICLE PREVIEW

a

Characteristic	N = 502,619 [†]
Variant	
E2:E2	2,336 (0.6%)
E2:E3	50,280 (12%)
E2:E4	10,456 (2.5%)
E3:E3	242,715 (59%)
E3:E4	97,598 (24%)
E4:E4	9,834 (2.4%)
Unknown	89,400
Sex	
Female	273,382 (54%)
Male	229,122 (46%)
Unknown	115
Tested	
Tested	77,221 (15%)
Result	
negative	60,659 (79%)
positive	16,562 (21%)
Origin	
outpatient	32,668 (42%)
inpatient	44,553 (58%)

[†] n (%)

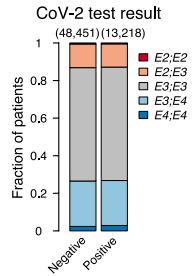
b



Characteristic	ARIC, N = 6,043 [†]	UKB, N = 402,763 [†]	p-value [‡]
Variant			
E2:E2	41 (0.7%)	2,336 (0.6%)	0.2
E2:E3	793 (13%)	50,280 (12%)	
E3:E3	3,648 (60%)	242,715 (60%)	
E3:E4	1,434 (24%)	97,598 (24%)	
E4:E4	127 (2.1%)	9,834 (2.4%)	

[†] n (%)
[‡] Pearson's Chi-squared test

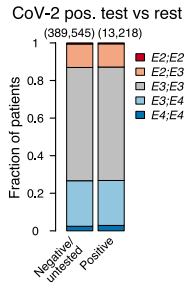
c



Characteristic	OR [†]	95% CI [†]	p-value
Variant			
E3:E3	—	—	
E2:E2	0.88	0.67, 1.15	0.4
E2:E3	0.98	0.92, 1.04	0.5
E3:E4	0.99	0.94, 1.04	0.6
E4:E4	1.21	1.08, 1.37	0.001

[†] OR = Odds Ratio, CI = Confidence Interval

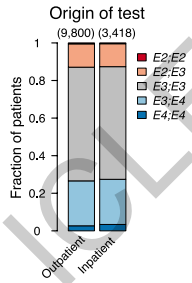
d



Characteristic	OR [†]	95% CI [†]	p-value
Variant			
E3:E3	—	—	
E2:E2	0.84	0.65, 1.07	0.2
E2:E3	0.99	0.93, 1.04	0.6
E3:E4	0.99	0.94, 1.03	0.5
E4:E4	1.18	1.06, 1.31	0.002

[†] OR = Odds Ratio, CI = Confidence Interval

e



Characteristic	OR [†]	95% CI [†]	p-value
Variant			
E3:E3	—	—	
E2:E2	0.98	0.79, 1.22	0.8
E2:E3	0.99	0.94, 1.04	0.7
E3:E4	1.00	0.96, 1.04	>0.9
E4:E4	1.06	0.96, 1.18	0.3

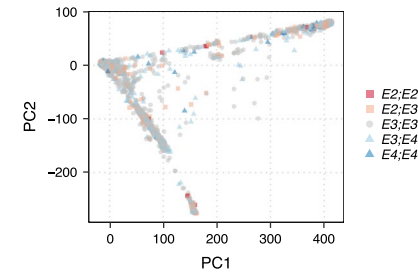
[†] OR = Odds Ratio, CI = Confidence Interval

Extended Data Fig. 7

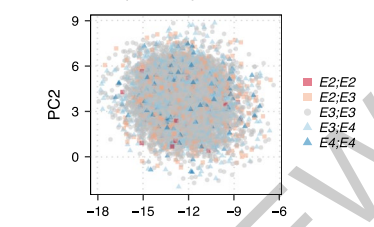
a Multivariate analysis UK Biobank

Variable	n	HR	p
Age	13207	1.163 (1.148, 1.177)	2.3e-123
Sex			
Female	6979	Reference	
Male	6228	1.926 (1.635, 2.268)	4.2e-15
PC1	13207	1.002 (1.001, 1.003)	0.00028
PC2	13207	0.999 (0.996, 1.002)	0.44
PC3	13207	1.002 (0.997, 1.006)	0.43
PC4	13207	0.997 (0.991, 1.004)	0.44
PC5	13207	0.989 (0.978, 1.001)	0.07
PC6	13207	0.987 (0.958, 1.016)	0.38
PC7	13207	0.990 (0.976, 1.005)	0.18
PC8	13207	1.006 (0.985, 1.027)	0.58
PC9	13207	0.998 (0.980, 1.016)	0.82
PC10	13207	0.988 (0.973, 1.003)	0.10
Genotype			
E3,E3	7973	Reference	
E2,E2	65	1.629 (0.673, 3.941)	0.28
E2,E3	1629	1.101 (0.865, 1.401)	0.44
E3,E4	3161	1.036 (0.856, 1.252)	0.72
E4,E4	379	2.220 (1.602, 3.076)	1.7e-06

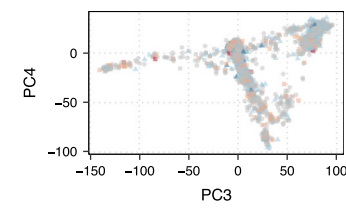
b Principal components 1–2



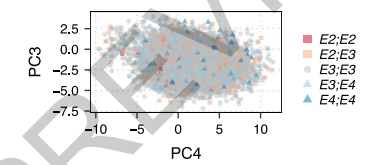
d Principal components 1–2



c Principal components 3–4



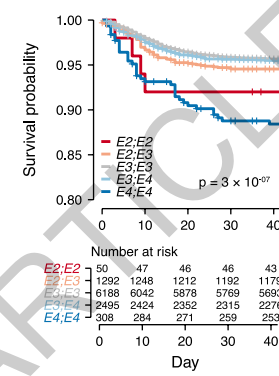
e Principal components 3–4



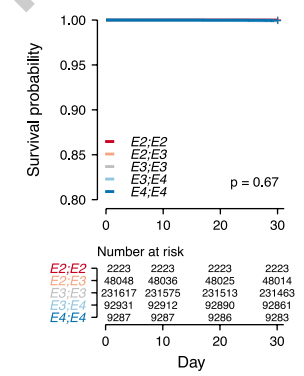
f Multivariate analysis UK Biobank

Variable	n	HR	p
Age	10333	1.164 (1.147, 1.181)	6.05e-93
Sex			
Female	5475	Reference	
Male	4858	1.967 (1.637, 2.365)	5.7e-13
Genotype			
E3,E3	6188	Reference	
E2,E2	50	1.561 (0.581, 4.190)	0.4
E2,E3	1292	1.244 (0.961, 1.610)	0.1
E3,E4	2495	1.000 (0.805, 1.242)	1.0
E4,E4	308	2.313 (1.626, 3.289)	3.1e-06

g APOE genotype



h Survival pre-pandemic



Extended Data Fig. 8

Reporting Summary

Nature Portfolio wishes to improve the reproducibility of the work that we publish. This form provides structure for consistency and transparency in reporting. For further information on Nature Portfolio policies, see our [Editorial Policies](#) and the [Editorial Policy Checklist](#).

Please do not complete any field with "not applicable" or n/a. Refer to the help text for what text to use if an item is not relevant to your study. [For final submission](#): please carefully check your responses for accuracy; you will not be able to make changes later.

Statistics

For all statistical analyses, confirm that the following items are present in the figure legend, table legend, main text, or Methods section.

n/a Confirmed

- The exact sample size (n) for each experimental group/condition, given as a discrete number and unit of measurement
- A statement on whether measurements were taken from distinct samples or whether the same sample was measured repeatedly
- The statistical test(s) used AND whether they are one- or two-sided
Only common tests should be described solely by name; describe more complex techniques in the Methods section.
- A description of all covariates tested
- A description of any assumptions or corrections, such as tests of normality and adjustment for multiple comparisons
- A full description of the statistical parameters including central tendency (e.g. means) or other basic estimates (e.g. regression coefficient) AND variation (e.g. standard deviation) or associated estimates of uncertainty (e.g. confidence intervals)
- For null hypothesis testing, the test statistic (e.g. F , t , r) with confidence intervals, effect sizes, degrees of freedom and P value noted
Give P values as exact values whenever suitable.
- For Bayesian analysis, information on the choice of priors and Markov chain Monte Carlo settings
- For hierarchical and complex designs, identification of the appropriate level for tests and full reporting of outcomes
- Estimates of effect sizes (e.g. Cohen's d , Pearson's r), indicating how they were calculated

Our web collection on [statistics for biologists](#) contains articles on many of the points above.

Software and code

Policy information about [availability of computer code](#)

Data collection Nikon NIS elements v5.20.02, QuantStudio Design & Analysis (v1.4.3), FACSDiva v8 (BD Biosciences), cellSens Dimension software (v1.16).

Data analysis Weight and survival of mice were analyzed in RStudio v1.4 using R v4.1.0 and the R packages 'survival' (v3.2), 'survminer' (v0.4.9), 'forestmodel' (v0.6.2), 'ggpubr' (v0.4.0), and 'tidyverse' (v1.3.1). qPCR data were analyzed in QuantStudio Design & Analysis (v1.4.3); immunofluorescence images were acquired using Nikon NIS elements (v5.20.02) and analyzed using CellProfiler (v4.2.1). RNA-seq data were analyzed using BBDuk (v38.9), STAR (v2.7.8a), R (v4.1.0), and DESeq2 (v1.32.0). For weighted gene co-expression analysis the R package WGCNA (v1.70) was used. scRNAseq data were analyzed using ParseBiosciences pipeline v0.9.6p and Seurat v4.0.2. GSEA was performed using the clusterProfiler package (v4.0.0). Analysis of human data was performed using PLINK v1.9 and downstream analysis was performed using the same tools as for mouse data described above. Summary tables were compiled using the R package 'gtsummary' (v1.4.1). Flow cytometry data were analyzed using Flowjo v9.3.

Computer code: All custom code is publicly available at https://github.com/benostendorf/ostendorf_et al_2022

For manuscripts utilizing custom algorithms or software that are central to the research but not yet described in published literature, software must be made available to editors and reviewers. We strongly encourage code deposition in a community repository (e.g. GitHub). See the Nature Portfolio [guidelines for submitting code & software](#) for further information.

Data

Policy information about [availability of data](#)

All manuscripts must include a [data availability statement](#). This statement should provide the following information, where applicable:

- Accession codes, unique identifiers, or web links for publicly available datasets
- A description of any restrictions on data availability
- For clinical datasets or third party data, please ensure that the statement adheres to our [policy](#)

Bulk RNA-seq and scRNA-seq data have been deposited at the Gene Expression Omnibus (GEO) under accession numbers GSE184289 and GSE199498, respectively. All data from the UK Biobank is publicly available under www.ukbiobank.ac.uk. MSigDB is publicly available under <http://www.gsea-msigdb.org>. Source data is provided with this paper.

Field-specific reporting

Please select the one below that is the best fit for your research. If you are not sure, read the appropriate sections before making your selection.

- Life sciences Behavioural & social sciences Ecological, evolutionary & environmental sciences

Life sciences study design

All studies must disclose on these points even when the disclosure is negative.

Sample size	No statistical methods were used to predetermine sample sizes. The number of samples per group was empirically chosen based on estimates of intra-group variation (Leist et al., Cell, 2020) and expected effect size (Ostendorf et al., Nature Medicine, 2020).
Data exclusions	All mouse data were included in the manuscript. For bulk RNA-sequencing, two out of 88 samples were identified as outliers based on principal component and sample distance analysis (large euclidean distance from all other samples of the same condition) and SARS-CoV-2 MA10 transcript abundance (outlying low virus transcript detection) and excluded from analysis.
Replication	Experiments were generally performed at least twice and pooled where appropriate as outlined in the individual figure legends.
Randomization	Samples were allocated randomly if possible (no infection versus infection groups). For experiments with genetically modified mice, allocation was performed according to genotype and mice were sex- and age-matched. No other covariates systematically differed between groups.
Blinding	Investigators were blinded for data collection and analysis of histology and immunofluorescence stainings. Two experiments on mouse survival and mouse weight courses were performed with investigators blinded with regards to genotype, yielding comparable results to the whole animal cohort. No blinding was performed for the remaining in-vivo experiments due to cage labeling requirements.

Reporting for specific materials, systems and methods

We require information from authors about some types of materials, experimental systems and methods used in many studies. Here, indicate whether each material, system or method listed is relevant to your study. If you are not sure if a list item applies to your research, read the appropriate section before selecting a response.

Materials & experimental systems

n/a	Involved in the study
<input type="checkbox"/>	<input checked="" type="checkbox"/> Antibodies
<input type="checkbox"/>	<input checked="" type="checkbox"/> Eukaryotic cell lines
<input checked="" type="checkbox"/>	<input type="checkbox"/> Palaeontology and archaeology
<input type="checkbox"/>	<input checked="" type="checkbox"/> Animals and other organisms
<input checked="" type="checkbox"/>	<input type="checkbox"/> Human research participants
<input checked="" type="checkbox"/>	<input type="checkbox"/> Clinical data
<input checked="" type="checkbox"/>	<input type="checkbox"/> Dual use research of concern

Methods

n/a	Involved in the study
<input checked="" type="checkbox"/>	<input type="checkbox"/> ChIP-seq
<input type="checkbox"/>	<input checked="" type="checkbox"/> Flow cytometry
<input checked="" type="checkbox"/>	<input type="checkbox"/> MRI-based neuroimaging

Antibodies

Antibodies used

IF stainings: CD45 (polyclonal, Abcam, #ab10558, 1:750), SARS nucleocapsid (polyclonal, Novus Biological, 56576, 1:1000), SARS-CoV2 nucleocapsid (polyclonal, GTX135357, 1:1000), goat anti-rabbit Alexa Fluor 555 (polyclonal, ThermoFisher Scientific, A-21428, 1:200). Flow cytometry: CD45-BV785 (clone: 30-F11, cat#: 103149, supplier: BioLegend, dilution: 1:3,000), CD11b-FITC (M1/70, 101206, BioLegend, 1:1,000), Ly6G-PerCP/Cy5.5 (1A8, 127616, BioLegend, 1:1,000), Ly6C-BV711 (HK1.4, 128037, BioLegend, 1:10,000), I-A/I-E-PE (M5/114.15.2, 107607, BioLegend, 1:10,000), CD19-PB (6D5, 115526, BioLegend, 1:500), CD19-BV421 (6D5, 115549, BioLegend,

1:500), NK1.1-APC (PK136, 17-5941-82, eBiosciences, 1:500), CD4-BV605 (GK1.5, 100451, BioLegend, 1:300), CD8 α -AF700 (53-6.7, 100730, BioLegend, 1:1,000), BV421-labeled SARS-CoV-2 S 539-546 tetramer (NIH Tetramer Core Facility, 1:200).

Validation

Validation data of the antibodies listed above was performed by the manufacturers and is available at each manufacturer's website by searching under the provided catalog numbers. Antibodies for IF were validated by the manufacturers either by assessing cells known to express or not to express the target protein and cross-referencing the expression pattern with the available literature or by orthogonal validation using an antibody-independent strategy. Antibodies for flow cytometry were validated by specificity testing on 1-3 target cell types with either single- or multi-color analysis including positive and negative cell types. New lots were validated to perform with similar intensity (MFI) as assessed on both positive and negative populations and each lot product was validated by QC testing with a series of titration dilutions.

Eukaryotic cell lines

Policy information about [cell lines](#)

Cell line source(s)

VeroE6: ATCC (CRL-1586) and Ralph Baric (University of North Carolina at Chapel Hill); Huh-7.5: Charles Rice (Rockefeller University; Blight et al, J Virol, 2002, developed in the laboratory of Charles Rice); Caco-2: ATCC (HTB-37).

Authentication

No authentication was performed on the cell lines.

Mycoplasma contamination

Mycoplasma contamination was ruled out in all cell lines.

Commonly misidentified lines
(See [ICLAC](#) register)

None.

Animals and other organisms

Policy information about [studies involving animals](#); [ARRIVE guidelines](#) recommended for reporting animal research

Laboratory animals

Human APOE2, APOE3, and APOE4 mice were obtained from Taconic Biosciences. Both female and male mice were used between 7-46 weeks of age as indicated in the figures. Mice were housed in a controlled ambient temperature (20-25°C) and humidity (30-70%) environment with a 12 hour light-dark cycle.

Wild animals

No wild animals were used in this study.

Field-collected samples

No field-collected samples were used in this study.

Ethics oversight

All animal experiments were conducted in accordance with a protocol approved by the Institutional Animal Care and Use Committee at The Rockefeller University.

Note that full information on the approval of the study protocol must also be provided in the manuscript.

Flow Cytometry

Plots

Confirm that:

- The axis labels state the marker and fluorochrome used (e.g. CD4-FITC).
- The axis scales are clearly visible. Include numbers along axes only for bottom left plot of group (a 'group' is an analysis of identical markers).
- All plots are contour plots with outliers or pseudocolor plots.
- A numerical value for number of cells or percentage (with statistics) is provided.

Methodology

Sample preparation

PBMCs were obtained from mice by submandibular bleedings and red blood cells were lysed in ACK buffer as outlined in the methods section. Lungs were dissociated into single-cell suspensions using the lung dissociation kit and a gentleMACS dissociator (Milteny biotec) as outlined in the methods section.

Instrument

BD LSR Fortessa

Software

BD DIVA software v8 was used for data collection and Flowjo software v9.3 was used for data analysis.

Cell population abundance

No cell sorting was performed.

Gating strategy

Gating strategies were followed as outlined in Extended Data Fig 4. In brief, an initial gate based on basal scatter characteristics served to exclude debris followed by singlet gates based on FSC-H and SSC-H. Compensation was calculated using single color controls using Ultracomp compensation beads (ThermoFisher) for antibodies and amine-reactive beads for Zombie (ThermoFisher).

- Tick this box to confirm that a figure exemplifying the gating strategy is provided in the Supplementary Information.